ALMA MATER STUDIORUM - UNIVERSITÀ DI BOLOGNA

SCUOLA DI INGEGNERIA E ARCHITETTURA

Dipartimento di Informatica – Scienza e Ingegneria

Corso di Laurea Magistrale in INGEGNERIA INFORMATICA

TESI DI LAUREA
in
Sistemi Embedded Riconfigurabili M

Unsupervised Learning of Scene Flow

CANDIDATO:
Matteo Boschini

RELATORE:
Prof. Stefano Mattoccia

CORRELATORI:
Dott. Matteo Poggi
Dott. Fabio Tosi

Anno Accademico 2017/18

Sessione I

Table of Contents

1. Introduction

As Computer Vision-powered autonomous systems are increasingly deployed to solve problems in the wild, the case is made for developing visual understanding methods that are robust and flexible.

One of the most challenging tasks for this purpose is given by the extraction of scene flow, that is the dense three-dimensional vector field that associates each world point with its corresponding position in the next observed frame, hence describing its three-dimensional motion entirely. The recent addition of a limited amount of ground truth scene flow information to the popular KITTI dataset prompted a renewed interest in the study of techniques for scene flow inference, although the proposed solutions in literature mostly rely on computation-intensive techniques and are characterised by execution times that are not suited for real-time application.

In the wake of the recent widespread adoption of Deep Learning techniques to Computer Vision tasks and in light of the convenience of Unsupervised Learning for scenarios in which ground truth collection is difficult and time-consuming, this thesis work proposes the first neural network architecture to be trained in end-to-end fashion for unsupervised scene flow regression from monocular visual data, called *Pantaflow*. The proposed solution is much faster than currently available state-of-the-art methods and therefore represents a step towards the achievement of real-time scene flow inference.

2. State of the Art

2.1. Scene Flow

As innovative Computer Vision-powered applications, which have the potential to change the world we live in, are gaining increasing visibility, it is fundamental to develop flexible and reliable systems to let computers make sense of the world they "see".
For instance, it is essential to provide an autonomous vehicle with a robust understanding of how objects move within the three-dimensional space around it. This kind of motion information was first named *scene flow* by Vendula et al. in their seminal study [1] and described as the dense three-dimensional vector field that associates each world point with its corresponding position in the next observed frame. Even though such scene understanding seems very natural to a human being, this is by every mean a very difficult task, as it combines the complexity of computing correspondences with three-dimensional data that is both hard to acquire and process. In addition to *autonomous driving/piloting*, other tasks that would benefit from the availability of strong *scene flow* methods include *localisation*, *mapping*, environmental monitoring, *surveillance*, *robot control*.

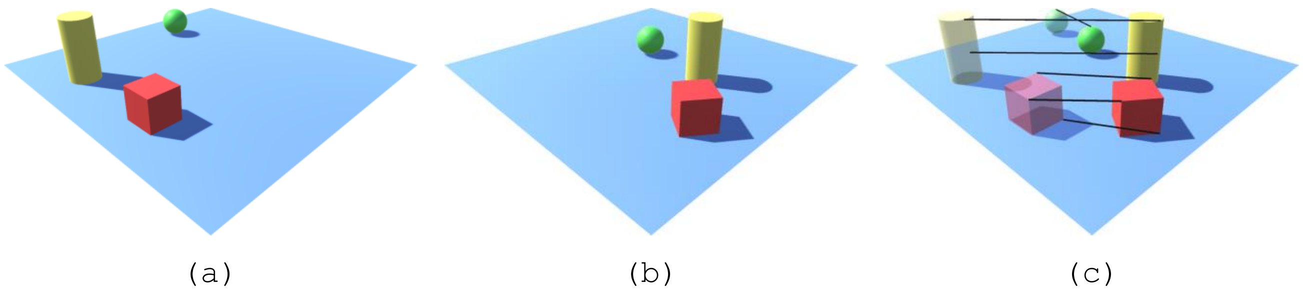

Figure 2.1 – (a) and (b) are subsequent frames in a simple 3D scene. We highlight in black in (c) some of the 3D vectors describing scene flow, connecting corresponding points in the objects.

Early studies [2, 18, 19, 20] on the subject relied on cost-intensive mathematical procedures such as *variational analysis*,

that are unfit for any real-time application. Additionally, in order to simplify data collection, many of these studies relied on synthetic datasets or on monocular or binocular data describing very simple and constrained scenes. The lack of reliability *in the wild* of models that were tuned on synthetic or otherwise controlled data is one of the main drivers behind the introduction of the *autonomous driving*-oriented KITTI benchmark [4] in 2012. Among the studies that were subsequently carried out to develop methods capable of handling this dataset, Vogel et al. [7] attempt tackling *scene flow* prediction by employing demanding and time-consuming matching techniques that deploy rigid models, making precise assumptions on camera velocity.
The 2015 extension to the KITTI dataset [13] was a major landmark in that, for the first time, it provided the scientific community with non-synthetic *scene flow* ground truth, although very limited in quantity. This is achieved by manually fitting geometrically accurate CAD models to the 3D point cloud that is acquired via laser scan, which is extremely expensive and time-consuming. Menze and Geiger supplement this new data with a *scene flow* prediction model that reasons about the structure of a driving scene, in that it interprets it as a collection of planar patches moving on a background. In [17], Behl et al. extend this method by also employing *recognition* and *segmentation*. Even though their work achieves currently state-of-the-art performance on the KITTI 2015 *scene flow* benchmark, the algorithm takes approximately ten minutes to process a single scene. A faster, although less precise, pipeline for *scene flow* estimate was presented by Taniai et al. in [12].

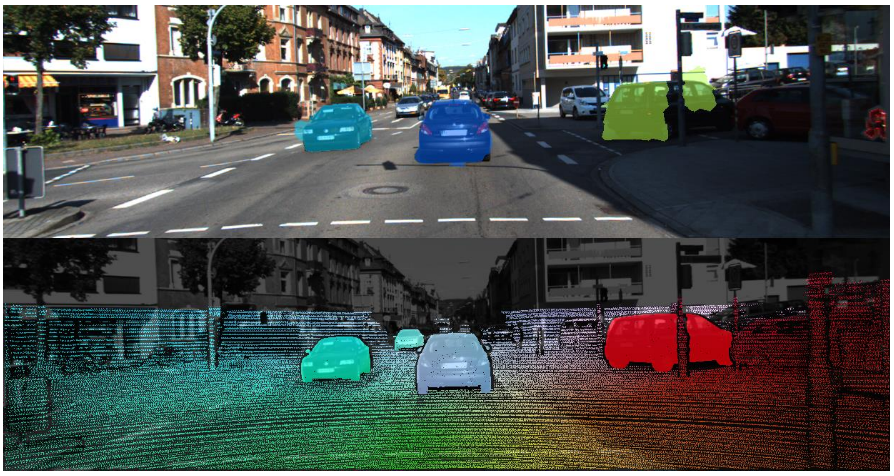

Figure 2.2 - An example of scene flow ground truth introduced in the 2015 extension to the KITTI dataset, picture taken from [13].

2.2. Deep Learning approaches for Stereo Matching and Optical Flow

Scene flow is possibly described as an extension of *Optical flow*, which is the establishment of two-dimensional motions of corresponding pixels in the image plane in succeeding frames. However, since it deals with three-dimensional information, it is also strongly related to *depth estimation*. In fact, in [2], Huguet and Devernay suggested that *scene flow* can be obtained as a combination of *optical flow* and *stereo matching*, as the latter allows to reconstruct pixel depth, to be combined with the motion information contained in the former.

The recent widespread adoption of *Deep Learning* approaches kickstarted many attempts to model *stereo matching* and *optical flow* as regression problems. Works like [10, 5, 6, 16] all put forward the employment of convolutional neural networks to infer these quantities. Zbontar and LeCun's proposal in [10] is the first attempt at stereo matching prediction on the original KITTI dataset with CNNs along with other optimisation techniques. A similar approach was then applied by Bai et al. in [16] to tackle *optical flow* regression. Dosovitskiy et al.'s *FlowNet*, proposed in [5], represents the first *end-to-end* architecture to be deployed for the same task. Ilg et al. propose *FlowNet 2.0* in [22], which is ultimately the result of several combined *FlowNet* instances, achieving accurate results in optical flow prediction, although it requires a delicate training schedule.

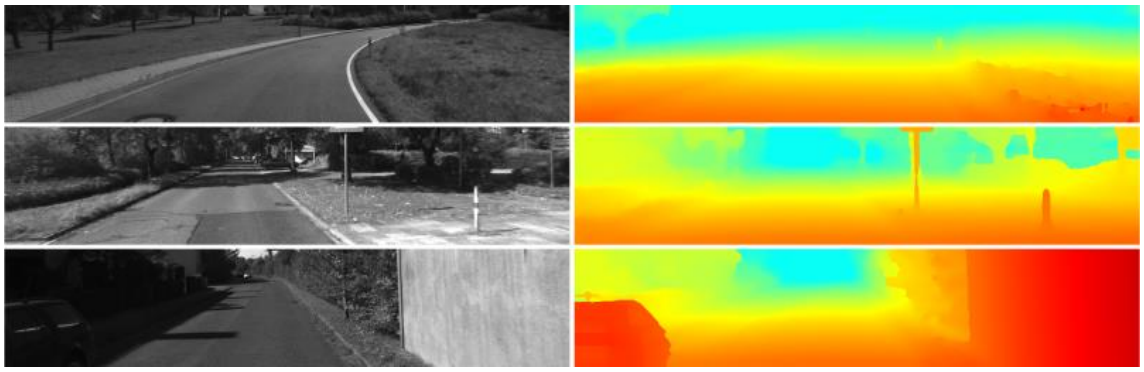

Figure 2.3 – An example of stereo matching inference by the means of CNNs, picture taken from [10].

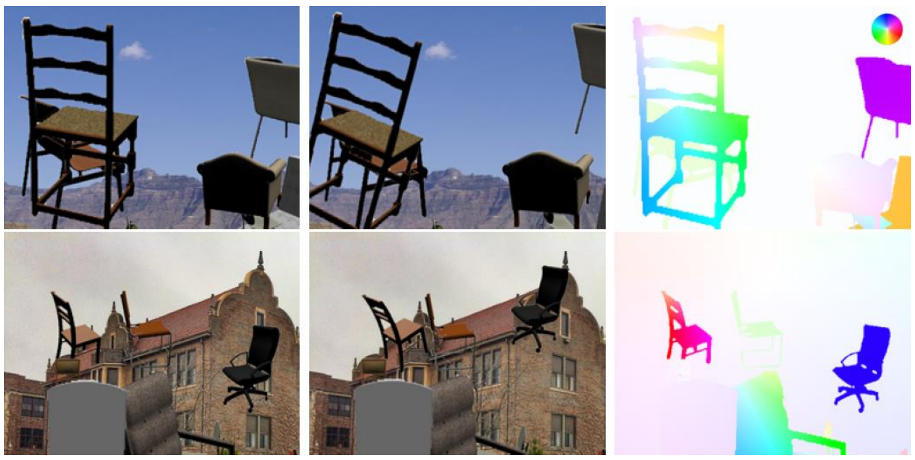

Figure 2.4 – An example of optical flow inference by FlowNet, picture taken from [5]. Note that optical flow vectors are graphically expressed via the Middlebury Colour code (see the colour wheel in the top-right coner).

Mayer et al.'s work [11] represents the first *Deep Learning*-based approach for *scene flow* inference. It works by combining *FlowNet* with two instances of a disparity-predicting network and fine tuning it all together. More recently, deep CNNs have also been used to assess the reliability of stereo matching by refining *confidence*

maps in [14], which can be subsequently used to improve stereo predictions made by stereo regression models, as shown in [15].
Deep Learning also allows for more sophisticated methods to be deployed, which are able to learn to infer disparity starting from a single image in a stereo pair in an unsupervised manner. Flynn et al. in [9] introduce a network that synthesises new views by using several input images. Xie et al. specifically tackle the challenge of monocular depth estimation in [26], using a model that computes a high number of candidate disparity values whose probability is then used to synthesise the missing element in the stereo pair. A very important contribution is made by Godard et al. in [3] by introducing a fully-differentiable neural network model called *Monodepth* for monocular depth estimation that can be trained in an *end-to-end* fashion. *Monodepth* learns to predict both the left-to-right and right-to-left disparity starting from a single image in the stereo pair and is trained by verifying the consistency between synthetic versions of the left and right images generated by warping the opposite one with the learned disparities and the actual images. Its operation is analysed in detail in chapter 2.3. Poggi et al. proposed [27] a lightweight model with comparable performance enabling real-time monocular depth estimation on standard CPU-based system and acceptable frame rate (e.g., 1 Hz) on embedded devices such as the Raspberry Pi 3.
A similar strategy is adopted by Meister et al. in [23] and by Wang et al. in [21] to achieve unsupervised learning of *optical flow* starting from unsupervised stereo pairs.
Among these very recent developments, at the time of this thesis, no published attempt has been made to introduce an *end-to-end* unsupervised model for *scene flow* inference.

2.3. Monodepth

2.3.1. Base architrecture

Godard et al.'s model in [3] constitutes the starting point for this thesis work. *Monodepth* is an Encoder/Decoder-structured CNN that aims at regressing disparity values starting from the left element l_0 of a rectified stereo pair. More precisely, l_0 is initially subject to multiple convolutional layers in the encoder, then the result is processed through the same number of *up-convolutional layers*, yielding two inferred disparity maps d_0^r and d_0^l, relative to the right and left element of the pair respectively. Input images are initially scaled to a 512x256 resolution, output maps are then extracted at this same scale at the last layer of the decoder and their scaled versions by factors $\frac{1}{2}$, $\frac{1}{4}$ and $\frac{1}{8}$, which are given as the output of the three preceding decoder layers, are also used to generate additional loss function gradient in the training procedure. Predictions are extracted at a given layer by applying an additional convolution with kernel size 3 and using a sigmoid as activation function.

The original codebase for *Monodepth* allows for the user to choose VGG's or ResNet's architecture for the encoder and – reversing it and using up-convolutions instead of convolutions – the decoder. By *up-convolutions*, we mean the combined application of upscaling and convolution with stride 1, whose result is effectively scaled up with respect to the input. All the experiments in this thesis were carried out using VGG, although they can be easily repeated using ResNet.

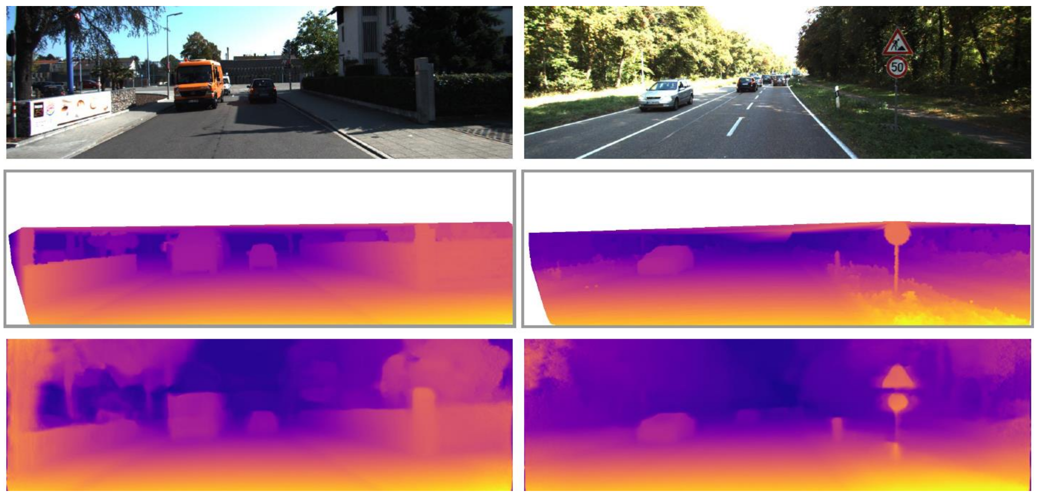

Figure 2.5 – An example of unsupervised monocular disparity prediction by Monodepth, picture taken from [3].

2.3.2. Training Procedure and Loss function

Monodepth's training is *unsupervised*, meaning that loss is not generated by comparing the networks' output with ground-truth disparity, but rather by working on an unmarked stereo pair. Three loss functions are computed for each of the two predictions and combined to yield the total loss for training. In the following, only losses relative to d_0^r will be described in detail. The corresponding terms for d_0^l can be obtained by simply swapping all occurrences of r and l.

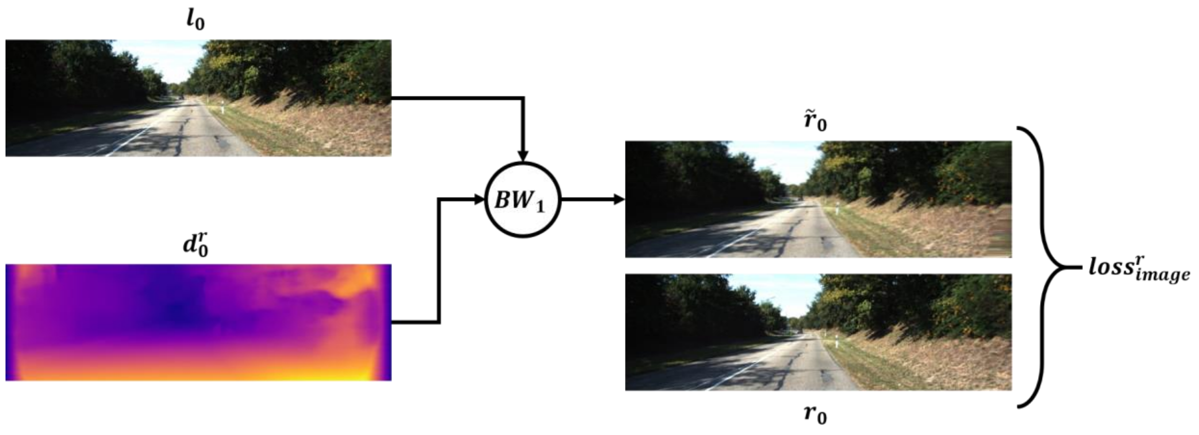

Figure 2.6 – A visual description showing how the right image is tentatively reconstructed by backward-warping the left image of the stereo pair with disparity. The discrepancy between the reconstructed right image and the original right image is the primary source of loss.

The total loss is mainly influenced by image loss, computed as shown in figure 2.6. A reconstruction $\tilde{r}_0$ of the right image can be obtained by backward-warping the left image l_0 according to the right inferred disparity d_0^r. If d_0^r matches the ground-truth disparity, $\tilde{r}_0$ will be identical to the actual right element of the pair r_0. Once again, it must be observed that leveraging this property does not ever require knowing any ground truth disparity. *Monodepth* is trained to minimise the dissimilarity between $\tilde{r}_0$ and r_0, which is measured with a combination of L1 and SSIM, as recommended in [6]. Let N be the number of pixels of the images and α be a coefficient between 0 and 1 (0.85 in *Godard et al.'s* code), the image loss term can be expressed with:

$$loss_{image}^{r} = \frac{1}{N}\sum_{i,j} \alpha \, \frac{1 - SSIM\big(\tilde{r}_0(i,j), r_0(i,j)\big)}{2} + (1-\alpha)\|\tilde{r}_0(i,j) - r_0(i,j)\|$$

A second order contribution to the overall loss is made by a loss function that is designed to keep the inferred disparities locally smooth. For this purpose, an L1 penalty is applied on the disparity gradients and weighted according to image gradients to introduce tolerance with respect to image edges (computed on a grayscale version of r_0), on which disparity is reasonably assumed to be discontinuous. Let ∂ indicate a gradient computed through central difference, we can express this loss term as:

$$loss_{smoothness}^{r} = \frac{1}{N}\sum_{i,j} |\partial_x d_0^r(i,j)| e^{-\|\partial_x r_0(i,j)\|} + |\partial_y d_0^r(i,j)| e^{-\|\partial_y r_0(i,j)\|}$$

A third loss term is designed to enforce consistency between the two predictions. For this purpose, the left inferred disparity d_0^l is backward-warped according to the right inferred disparity d_0^r, determining a reconstruction of this latter quantity, that we indicate as $\tilde{d}_0^r$. The actual loss term is given by the L1 difference between d_0^r and $\tilde{d}_0^r$:

$$loss_{consistency}^r = \frac{1}{N}\sum_{i,j} |d_0^r(i,j) - \tilde{d}_0^r(i,j)|$$

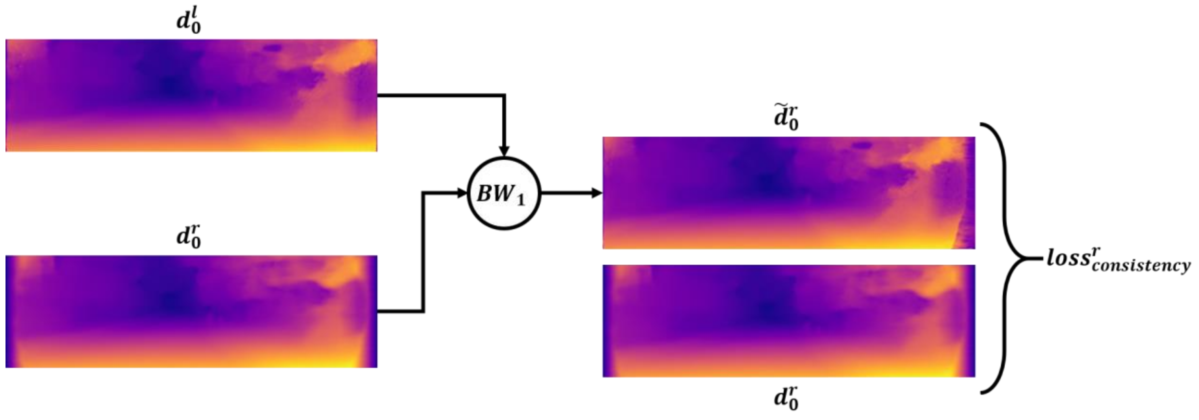

Figure 2.7 – A visual description showing the procedure for the computation of left-right consistency loss with respect to the right inferred disparity.

The total loss for each training sample is then given by the combination of all these contributions relative to both predictions and can be expressed as follows:

$$\begin{aligned} loss = \left(loss_{image}^l + loss_{image}^r\right) \cdot image_{weight} + \left(loss_{smoothness}^l + loss_{smoothness}^r\right) \\ \cdot smoothness_{weight} + \left(loss_{consistency}^l + loss_{consistency}^r\right) \cdot consistency_{weight} \end{aligned}$$

Weighting coefficients default at 1.0 for *image* and *consistency* terms and at 0.1 for the *smoothness* term.

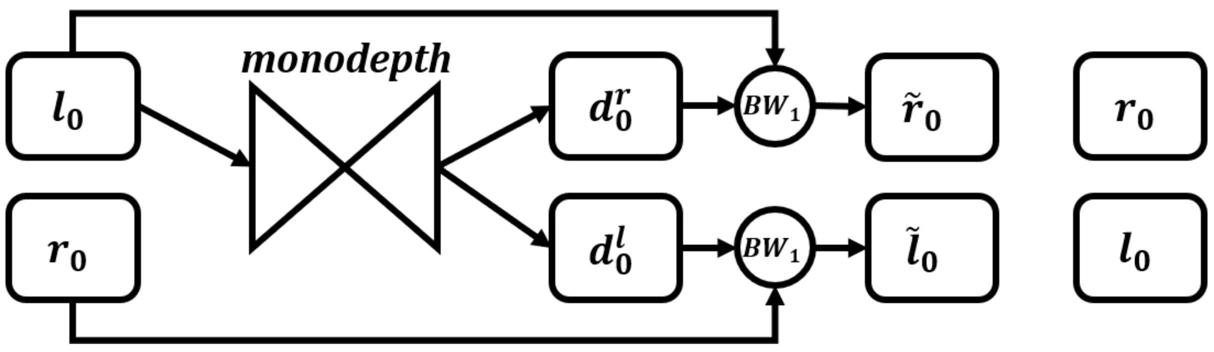

Figure 2.8 – A diagram showing how both the left and right items in a stereo pair are used for training (only the image loss is shown). Inference only depends on l_0.

Even though the training procedure requires both the initial left and right images, inference depends on l_0 alone, while r_0 is only used for the generation of loss. For this reason, we are not required to provide the right element of the stereo pair if we are just interested in inferring disparity, which makes it possible to obtain these predictions from very simple imaging setups, including generic smartphone cameras. Figure 2.9 shows some examples of depth inferences for images captured using a mobile phone camera.

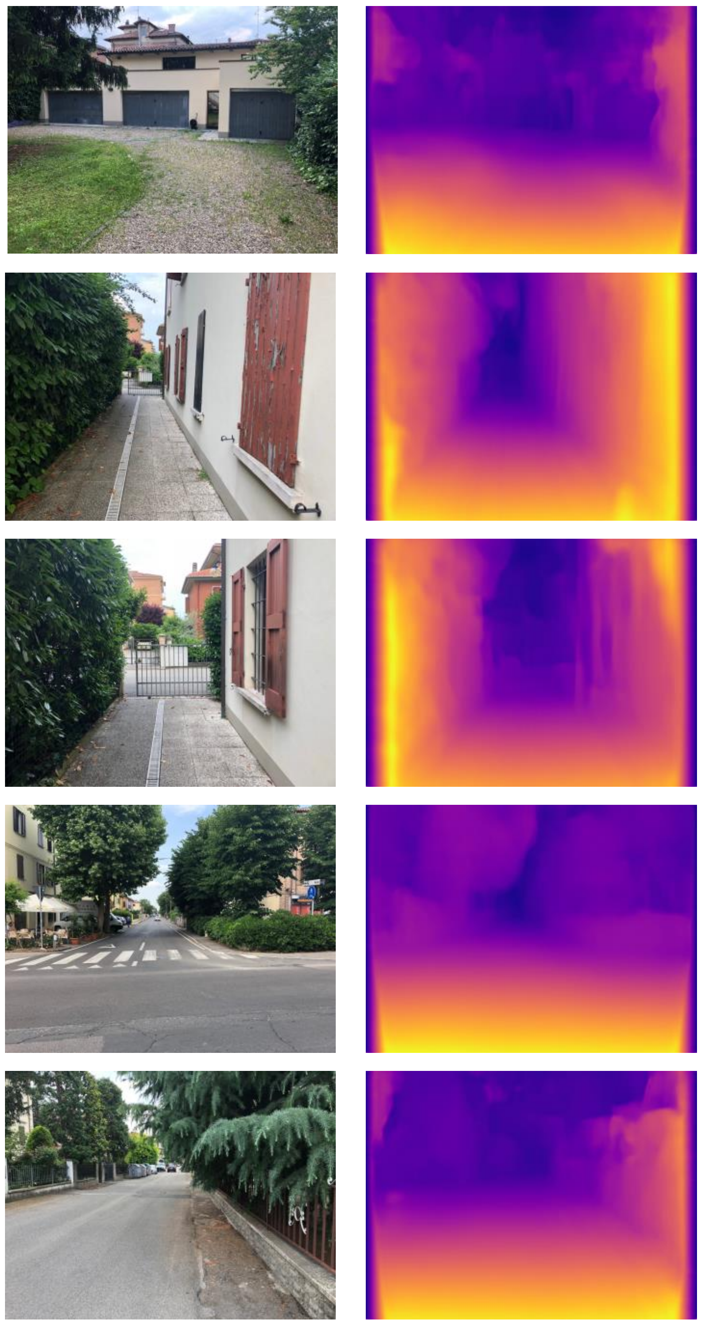

Figure 2.9 - Images captured from a smartphone and their disparity maps inferred through Monodepth.

3. Monoflow

Since the purpose of this thesis is producing an unsupervised methodology for scene flow inference, it is necessary to devise a procedure for optical flow prediction to work in synergy with *Monodepth*, thus allowing for the combination of disparity and optical flow information (as already mentioned in chapter 2.2).
Instead of relying on a different neural network model, the choice was made to carry out these predictions through a slightly modified version of *Godard et al.'s* architecture, repurposed to produce two-dimensional output, that will be referred to as *Monoflow*.

3.1. Architecture and Training

Instead of using a stereo pair, *Monoflow* is trained on a pair of subsequent monocular frames l_0 and l_1. Note that, unlike *Monodepth*, the new architecture uses both input images for the inference. This does reduce the portability of our solution at prediction-time, as they refer to the same camera and can therefore be assumed to be available on simple capture setups at prediction time.

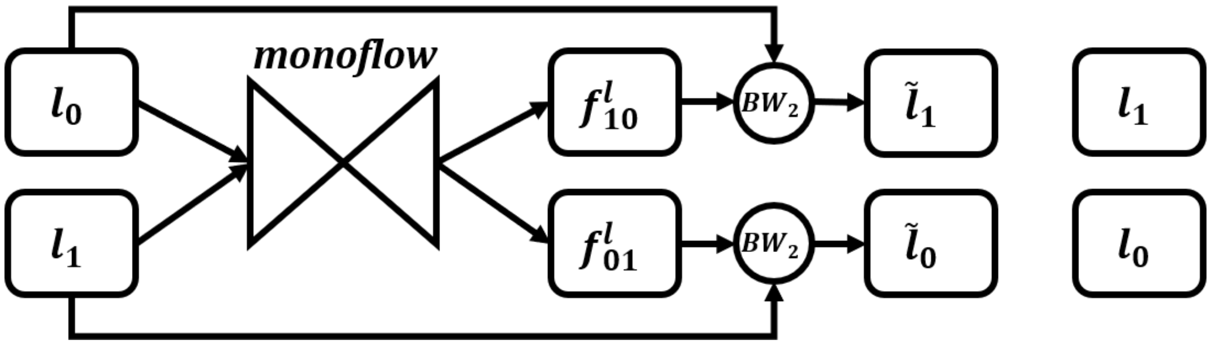

Figure 3.1 – A diagram showing how two subsequent frames referring to the same camera are used for training Monoflow *(only image loss is shown)*. Inference depends on both l_0 and l_1.

The network is still organised in an Encoder/Decoder structure, based on VGG. It must be noticed that, since optical flow conveys information about both horizontal and vertical displacements, out-

put predictions f_{01}^l and f_{10}^l will include two channels each. These two predictions correspond respectively to the forward flow that accounts for how points in l_0 move to their new positions in l_1 and to the backward flow, expressing how points in l_1 should move to go back to their positions in l_0. As pixels' movements may be positive and negative along each axis (unlike disparity), it is required to produce f_{01}^l and f_{10}^l through convolutional layers whose activation function is not exclusively positive. For this reason, sigmoidal activations were replaced by hyperbolic tangents in these layers.
The loss function used to train *Monoflow* is made up of three pairs terms (that refer both to the forward and backward flow), corresponding to the ones used for *Monodepth*:

$$loss = \left(loss_{image}^{01} + loss_{image}^{10}\right) \cdot image_{weight} + \left(loss_{smoothness}^{01} + loss_{smoothness}^{10}\right) \cdot smoothness_{weight} + \left(loss_{consistency}^{01} + loss_{consistency}^{10}\right) \cdot consistency_{weight}$$

In the following, we will only describe loss terms relating to backward flow f_{10}^l. The corresponding formulae for forward flow terms can be obtained by swapping all occurrences of *0* and *1* in the symbols.

The smoothness term applies an L1 penalty on the gradient of the optical flow prediction, weighted by the image gradient to introduce tolerance with respect to grayscale image discontinuities (f_{10}^l refers to l_1). Loss terms are initially computed for each optical flow channel separately and the overall result is given by their average.

$$loss_{smoothness_x}^{10} = \frac{1}{N}\sum_{i,j} \left|\partial_x f_{10}^l(i,j)_x\right| e^{-\|\partial_x l_1(i,j)\|} + \left|\partial_y f_{10}^l(i,j)_x\right| e^{-\|\partial_y l_1(i,j)\|}$$

$$loss_{smoothness_y}^{10} = \frac{1}{N}\sum_{i,j} \left|\partial_x f_{10}^l(i,j)_y\right| e^{-\|\partial_x l_1(i,j)\|} + \left|\partial_y f_{10}^l(i,j)_y\right| e^{-\|\partial_y l_1(i,j)\|}$$

$$loss_{smoothness}^{10} = \frac{loss_{smoothness_x}^{10} + loss_{smoothness_y}^{10}}{2}$$

Consistency and image terms require the application of backward warping with f_{10}^{l} to reconstruct images. Backward warping must displace pixels both vertically and horizontally, whereas in *Monodepth* it only worked horizontally. By warping the forward optical flow f_{01}^{l} according to f_{10}^{l}, we obtain an expression of the forward flow relative to pixel positions of f_{10}^{l}, that we indicate as $\tilde{f}_{10}^{l}$ (see figure 3.2). As these two quantities are expected to be opposite, the consistency loss term is given by the average absolute value of the sum between f_{10}^{l} and $\tilde{f}_{10}^{l}$:

$$loss_{consistency}^{10} = \frac{1}{N}\sum_{i,j} |f_{10}^{l}(i,j) + \tilde{f}_{10}^{l}(i,j)|$$

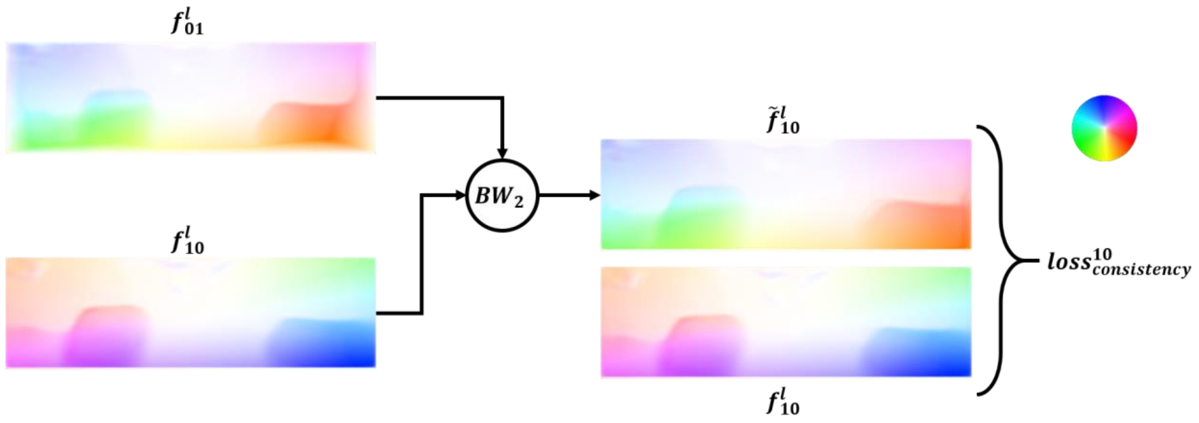

Figure 3.2 – A visual description showing the procedure for the computation of left-right consistency loss with respect to the right inferred disparity. The correspondence between colour hue and motion direction can be inferred from the colour wheel.

To generate the image loss term used in *Monoflow's* training, a comparison is made between the reconstruction of I_1 that is obtained by backward-warping I_0 according to f_{10}^{l}, that is $\tilde{I}_1$, and I_1 itself (see figure 3.3). In addition to the comparison methodology applied in by *Godard et al.*, combining L1 and SSIM distances, a second distance measure based on Ternary census Transform can also be used as suggested in [23]. Both formulae for the image loss term are listed in the following; please refer to chapter 3.2 for a detailed explanation of the second possibility.

$$loss^{10}_{image_{L1/SSIM}} = \frac{1}{N}\sum_{i,j} \alpha \, \frac{1 - SSIM\left(\tilde{l}_1(i,j), l_1(i,j)\right)}{2} + (1-\alpha)\|\tilde{l}_1(i,j) - l_1(i,j)\|$$

$$loss^{10}_{image_{TCT}} = \frac{1}{N}\sum_{i,j} \rho\left(\Delta_{NSH}\left(TCT\left(\tilde{l}_1(i,j)\right), TCT(l_1(i,j))\right)\right)$$

Where TCT is the Ternary census Transform, Δ_{NSH} is the Normalised Squared Hamming Distance and ρ is the Charbonnier Penalty Function (see chapter 3.2.3). In our training for *Monoflow*, we employ the latter formulation for image loss and always resort to the Ternary census Transform.

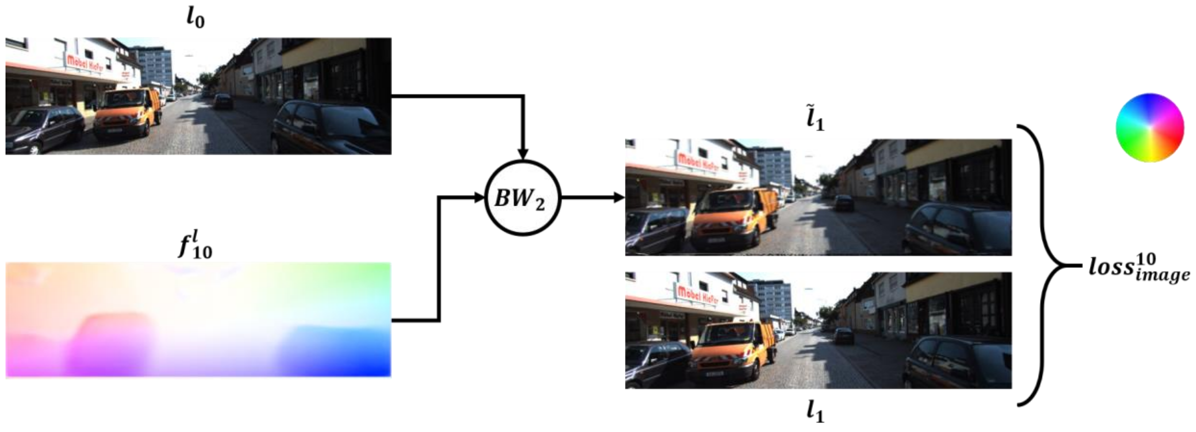

Figure 3.3 – A visual description showing how the second frame is tentatively reconstructed by backward-warping the first frame with backward flow. The discrepancy between the reconstructed and the original image is the primary source of loss.

As qualitatively illustrated by the results in figure 3.4, *Monoflow* appears to be effective at optical flow prediction and requires a training routine that is much simpler than the one of *Flownet* [5, 22], which is one of the most popular deep-learning architectures for optical flow regression.

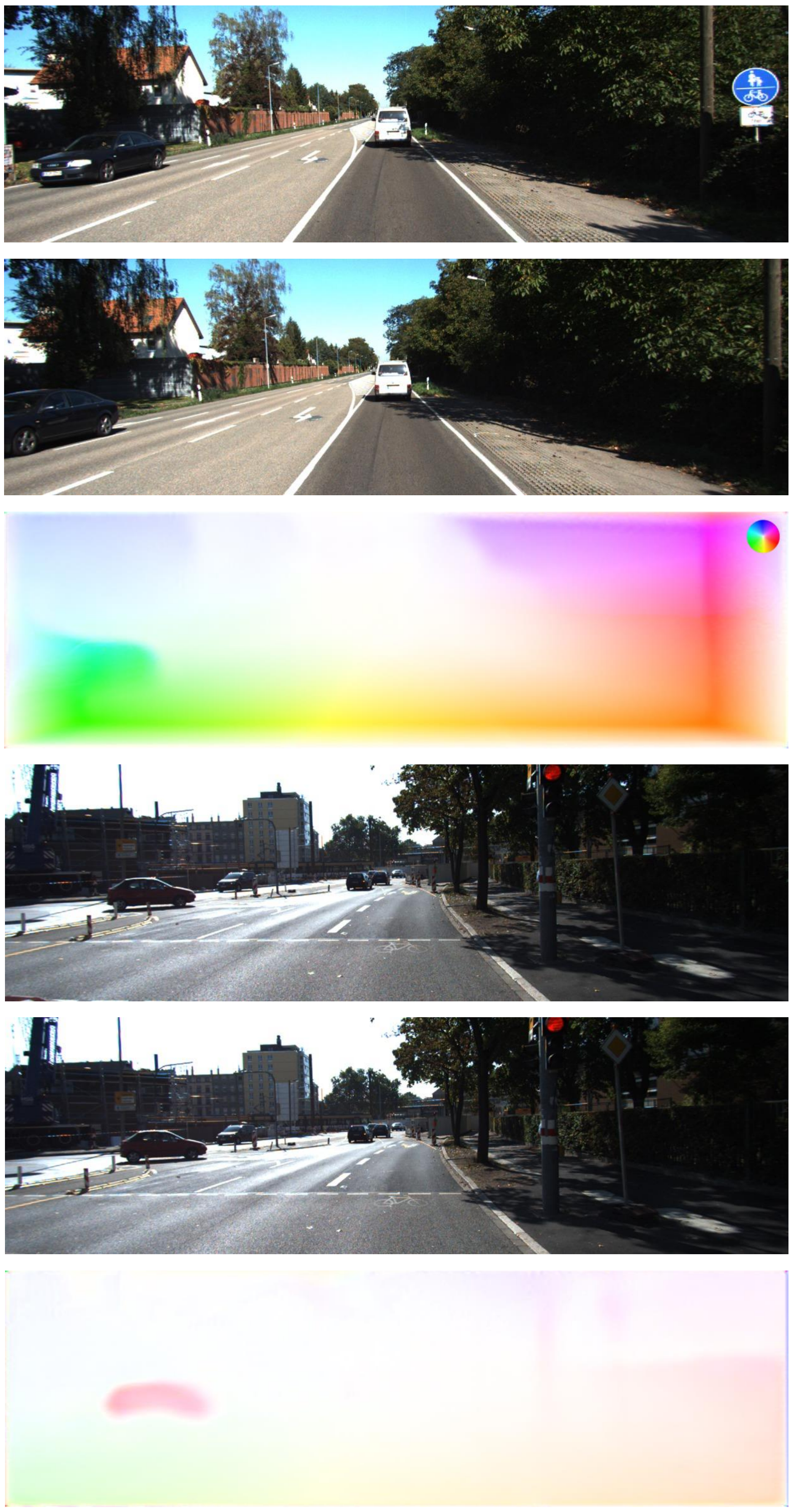

Figure 3.4 – Examples of optical flow inferences made by Monoflow *on images coming from the KITTI dataset.*

3.2. Census Transform

The newly introduced formulation for the image loss term is inspired by the work of *Meister et al.* in [23]. It relies on the generation of a descriptor for each pixel in the images to be compared, which summarises information about its neighbourhood in a bit string.

3.2.1. Census Transform

The census Transform was first proposed by Zabih and Woodfill in [8] as a non-parametric local transform to tackle the correspondence problems by highlighting the relation between intensity values in adjacent pixels.

Let ξ be a binary function of two grey level values, defined as follows:

$$\xi(P,P') = \begin{cases} 0 & if\ P > P' \\ 1 & if\ P \leq P' \end{cases}$$

Let $I(i,j)$ denote the grey level of the pixel at position (i,j) in image I, let D be a set of displacements that we use to express its neighbourhood, the Census Transform of $I(i,j)$ produces a bit string according to the following formula:

$$R_\tau\big(I(i,j)\big) = \underset{k,l \in D}{\#\#} \xi\big(I(i,j), I(i+k, j+l)\big)$$

where ## denotes concatenation. The resulting bit string is as long as the number of displacements contained in D.

For instance, consider the following 3x3 image region.

$$\begin{matrix} 127 & 128 & 129 \\ 126 & \mathbf{128} & 129 \\ 127 & 131 & 129 \end{matrix}$$

The census Transform for the central element with respect to its 8-neighbourhood (visited from left to right and from top to bottom) is given by the linearization of the applications of ξ to the central pixel and each other pixel in the neighbourhood:

$$R_\tau(\mathbf{128}) = \xi\begin{pmatrix} 127 & 128 & 129 \\ 128, 126 & n/a & 129 \\ 127 & 131 & 129 \end{pmatrix} = \begin{matrix} 0 & 1 & 1 \\ 0 & n/a & 1 \\ 0 & 1 & 1 \end{matrix} \xRightarrow{as\ string} [0,1,1,0,1,0,1,1]$$

The resulting bit string is highly informative of the local geometry for the image (let m be the cardinality of D, it allows for up to 2^m different patches to be represented) and yet very simple to compute. As only local relations between pixels are inquired, the resulting representation is invariant to changes in gain or bias.
In [8], the Transform is used to determine whether two patches are similar by computing the Hamming Distance between their bit strings.

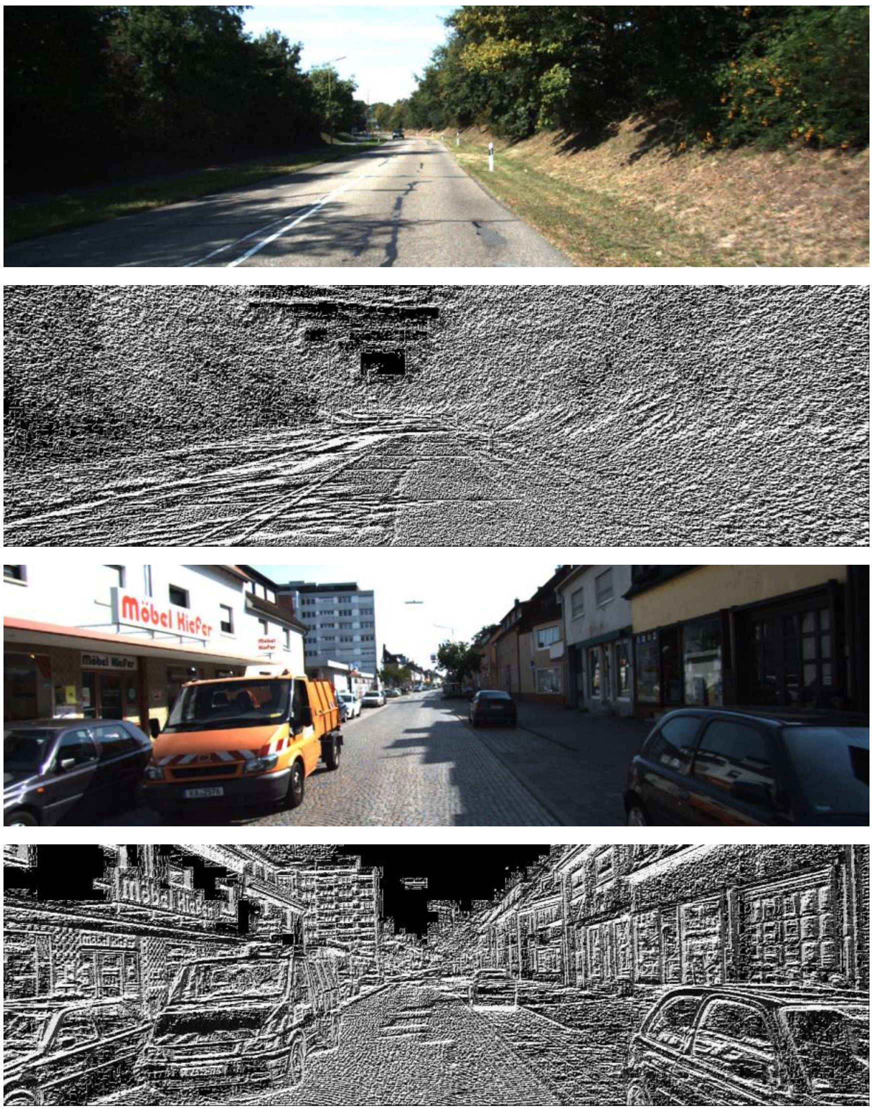

Figure 3.5 – Examples of the application of the census Transform on KITTI images. The resulting bit strings are converted to grey level values (different levels mean different strings).

3.2.2. Ternary census Transform

In [18], Stein modifies the original census Transform proposal by replacing ξ with the following ternary function ξ_3 which employs an additional parameter ϵ called census:

$$\xi_3(P,P') = \begin{cases} -1 & if\ P - P' > \varepsilon \\ 0 & if\ |P - P'| \leq \varepsilon \\ 1 & if\ P' - P > \varepsilon \end{cases}$$

The introduction of ε allows for additional information to be gathered, explicitly describing the situation in which the grey levels of P and P' are similar. The Ternary census Transform can therefore be expressed as:

$$R_{\tau_3}\big(I(i,j)\big) = \underset{k,l\in D}{\#\#} \xi_3\big(I(i,j), I(i+k, j+l)\big)$$

Note that, while all the advantages that come from the employment of relative intensities between pixels are inherited by the Ternary Transform, the discriminative power of the resulting description string is higher, as we can represent 3^m different patches.
The value we choose for census determines how sensitive the transform is to noise. For instance, choosing $\varepsilon = 0$ means that even minimal noise alters the descriptions consistently, while $\varepsilon = grey_{max}$ makes the descriptor insensitive to any kind of intensity variation. Stein recommends choosing $\varepsilon = 16$ for common 8-bit images.

Consider the following example 3x3 image region.

$$\begin{matrix} 124 & 74 & 32 \\ 124 & \mathbf{64} & 18 \\ 157 & 116 & 84 \end{matrix}$$

If we assume that $\varepsilon = 16$, the Ternary census Transform for the central element with respect to its 8-neighbourhood (visited from left to right and from top to bottom) is given by:

$$R_{\tau_3}(\mathbf{64}) = \xi_3\left(64, \begin{matrix} 124 & 74 & 32 \\ 124 & n/a & 18 \\ 157 & 116 & 84 \end{matrix}\right) = \begin{matrix} 1 & 0 & -1 \\ 1 & n/a & -1 \\ 1 & 1 & 1 \end{matrix} \xrightarrow{as\ string} [1, 0, -1, 1, -1, 1, 1, 1]$$

With respect to the binary descriptor, storing the ternary string requires encoding the tree values. This means that twice as much computer memory as in the precious case is needed, as the three possible values must be encoded with the following 2-bit combinations:

$$\begin{cases} -1 = 00 \\ 0 = 01 \\ 1 = 11 \end{cases}$$

Although more efficient encodings could be devised (e.g. storing the most frequent value with a single bit and the others with two), the one specified above is still preferred as the distance between the two opposite values -1 and 1 is maximised as far as Hamming Distance is concerned.

The descriptor string from the example above could then be encoded in 16 bits as $[11, 01, 00, 11, 00, 11, 11, 11]$.

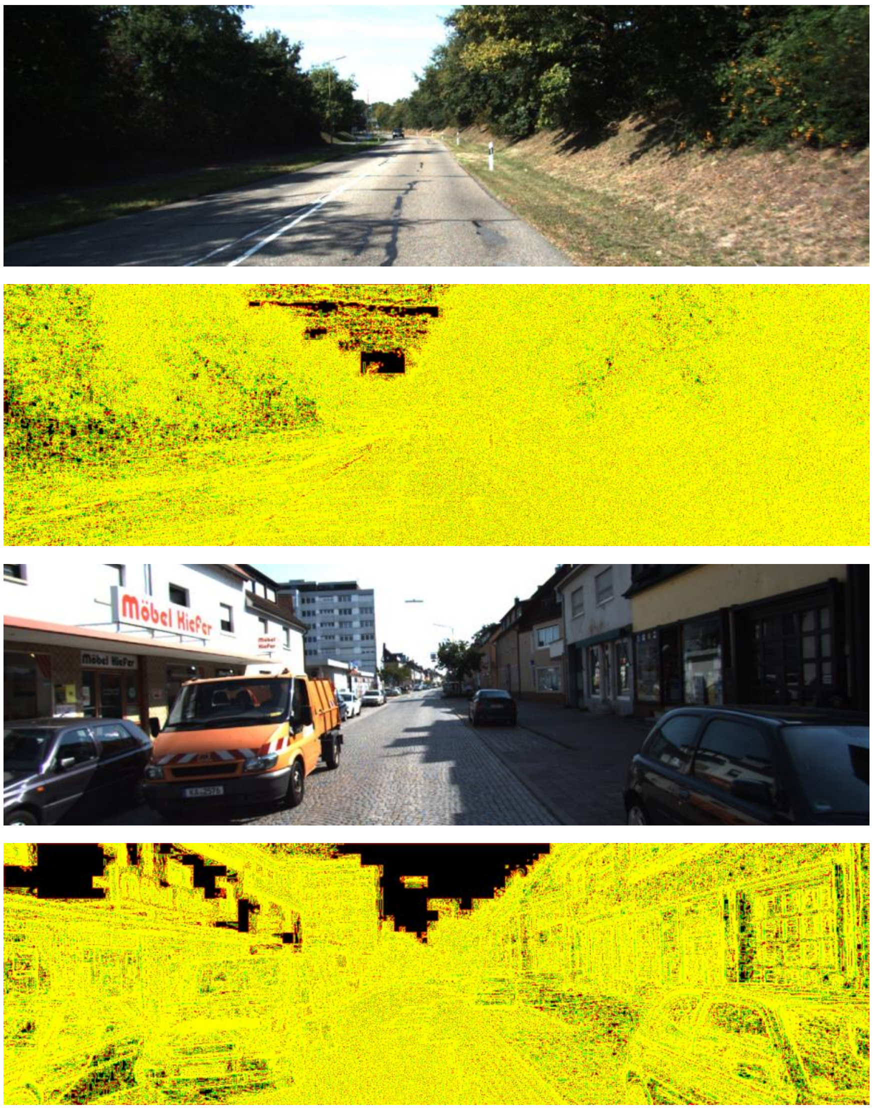

Figure 3.6 – Examples of the application of the Ternary census Transform on KITTI images. The resulting decoded bit strings are decoded to red and blue level values (different levels mean different strings).

3.2.3. Computing image loss

As anticipated in chapter 3.1, the Ternary census Transform can be used to compute a loss term accounting for the dissimilarity between an image I and its reconstruction $\tilde{I}$, as described in [23]:

$$loss^{I}_{image_{TCT}} = \frac{1}{N}\sum_{i,j} \rho\left(\Delta_{NSH}\left(TCT\left(\tilde{I}(i,j)\right), TCT(I(i,j))\right)\right)$$

I and $\tilde{I}$ are initially elaborated through the Ternary census Transform, yielding a descriptive ternary string for each Image pixel. These richer descriptions are pixel-wise compared through the Normalised Squared Hamming Distance $\Delta_{NSH}(S,S')$. Given two strings S and S' with length l, we define this function as:

$$\Delta_{NSH}(S,S') = \sum_{i=1}^{l} \frac{(S(i) - S'(i))^2}{0.1 + (S(i) - S'(i))^2}$$

where HD denotes simple Hamming Distance. As can be clearly seen in figure 3.7, employing Δ_{NSH} means introducing a huge penalty even in the case of small differences between the strings. This is further exemplified in figure 3.8, in which a visual comparison between the Hamming distance and Δ_{NSH} of two images is shown.

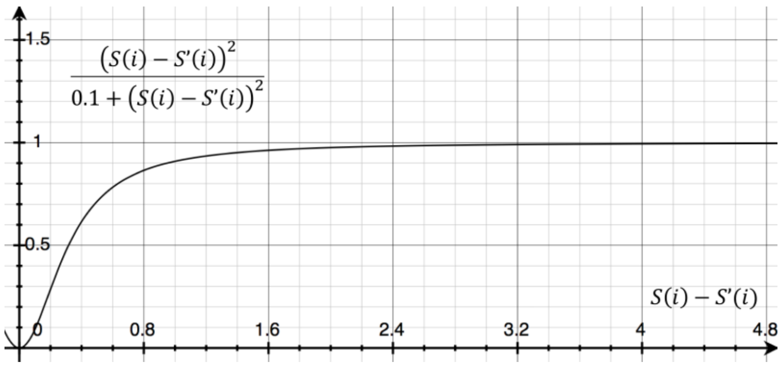

$\lvert S(i) - S'(i) \rvert$	$\frac{(S(i)-S'(i))^2}{0.1+(S(i)-S'(i))^2}$
0	0
1	0.9091
2	0.9756
3	0.9890
...	...

Figure 3.7 – Graph showing how Δ_{NSH}'s output relates to the Hamming Distance for a single string item. The comparison made by Δ_{NSH} is normalised between 0 and 1 and even small edit distances are related to a high penalty.

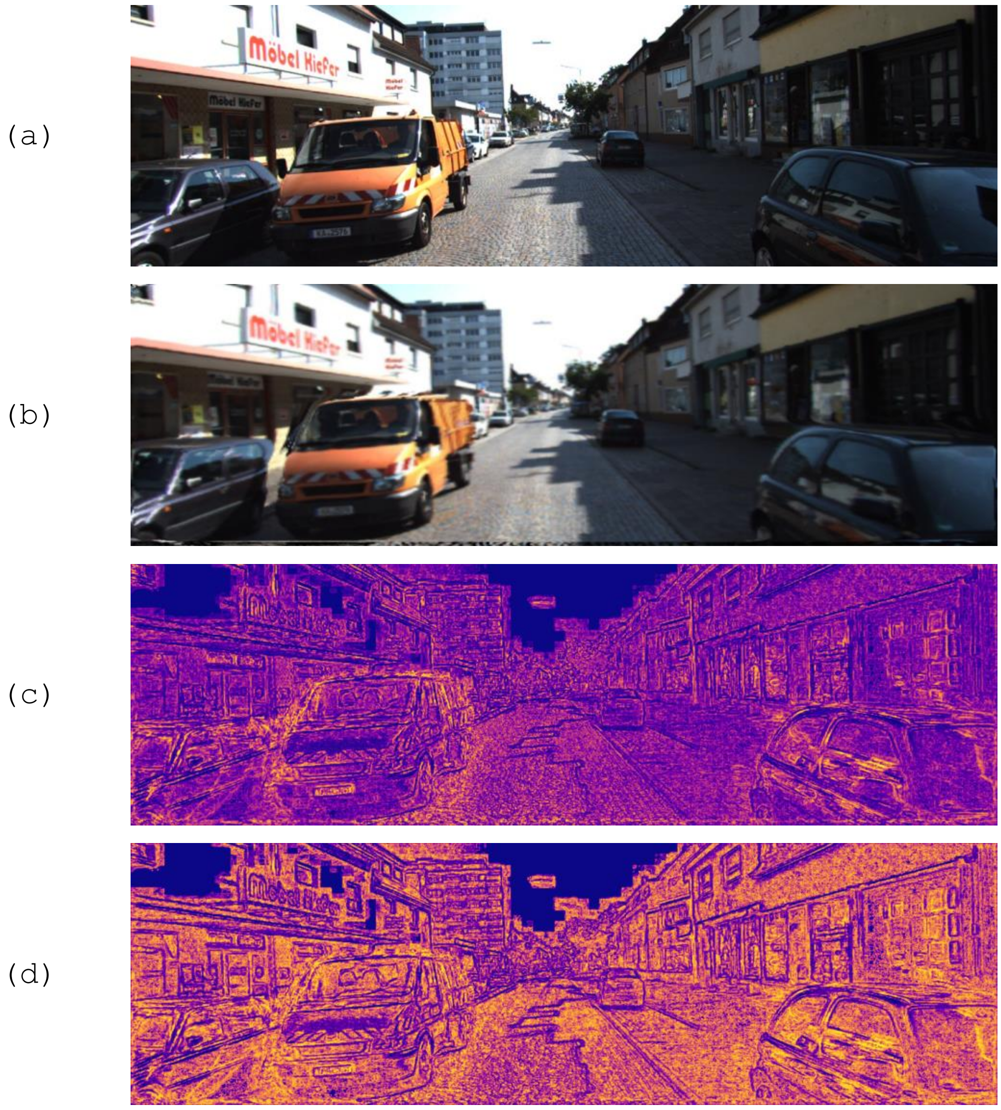

Figure 3.8 – An image from the KITTI dataset (a), its reconstruction with Monoflow (b) and a visual comparison between their Hamming Distance (c) and their Normalised Squared Hamming Distance (d).

The result of Δ_{NSH} is further elaborated through the robust Generalised Charbonnier Penalty Function ρ as described in [19] with:

$$\rho(x) = (x^2 + \varepsilon^2)^a$$

where $a = 0.45$ and ε small (in our code $\varepsilon = 0.001$). This function is a differentiable variant of the absolute value, as shown clearly in figure 3.9.

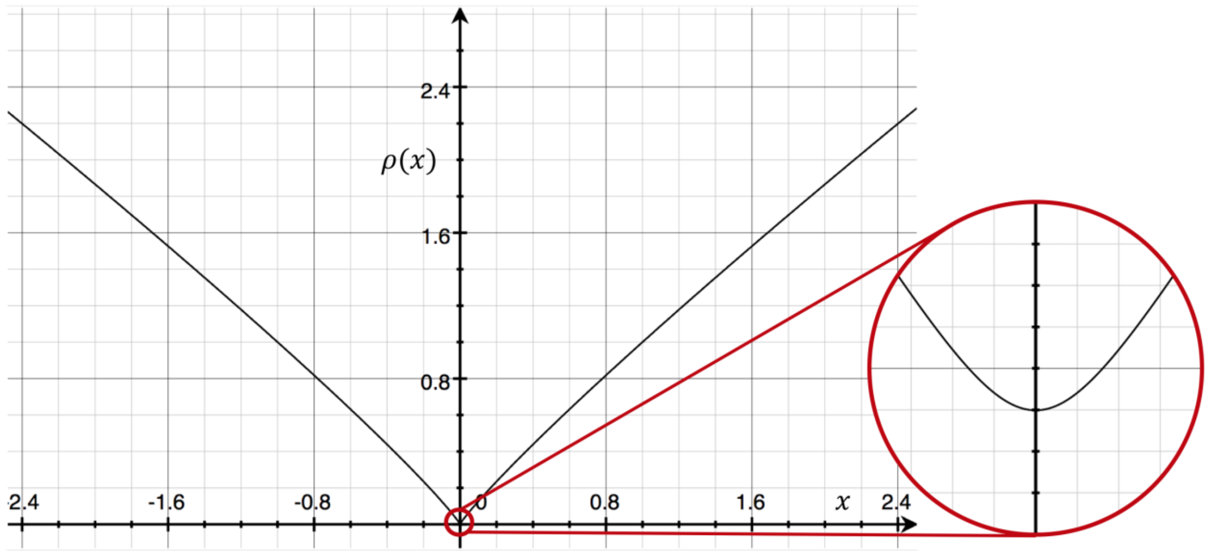

Figure 3.9 – Graph for the Generalised Charbonnier Penalty Function, including a fine zoom to highlight differentiability.

4. Pantaflow

4.1. Scene flow inference methods

While in chapter 3 we described the necessary modifications that were carried out on the initial *Monodepth* architecture to come up with a system for *optical flow* prediction, the present chapter deals with the definition of an unsupervised architecture for *scene flow* inference referred to as *Pantaflow*.

To understand the 3D motion of a scene point in space, we need to combine the information we have on its movement along the image plane (*optical flow*) with information on its translation along the orthogonal axis, which can be expressed as *disparity change*.

Given two consecutive frames l_0 and l_1, showing an object that moves in space, we can use *Monodepth* to infer the two corresponding disparity maps d_0^l and d_1^l. The difference between the disparity value that we observe for the same moving object in these maps allows us to determine how it moved along the orthogonal axis with respect to the camera plane. As the movement, however, also occurs along image plane, in order to make the two disparity maps easily comparable, one needs to be backward warped with optical flow (that can be inferred by *Monoflow*) so as to compensate movement along the image plane and obtain two "superimposable" maps that can be easily compared by the means of a simple difference.

With reference to the visual exemplification of this procedure in figure 4.1, the version of d_1^l that is warped to be made comparable with d_0^l is called $r_0 d_1^l$. By inverting the two disparity maps and using the opposite optical flow for warping, we can similarly obtain $r_1 d_0^l$. We will refer to $r_0 d_1^l$ and $r_1 d_0^l$ as relative disparity maps.

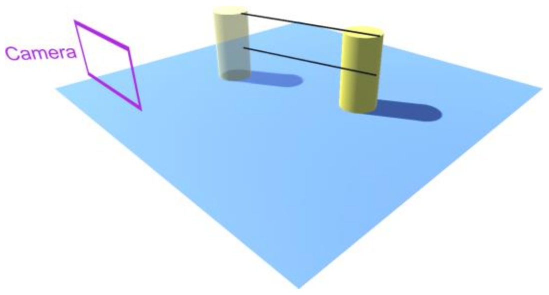

(a)

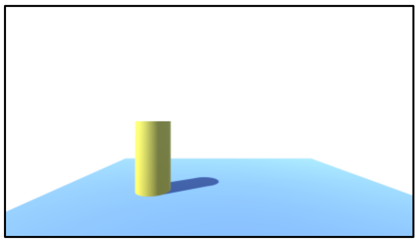

(b)

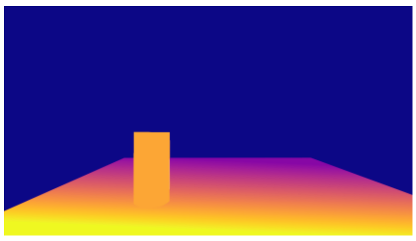

(c)

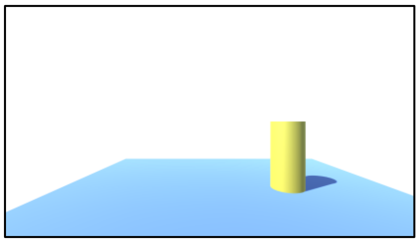

(d)

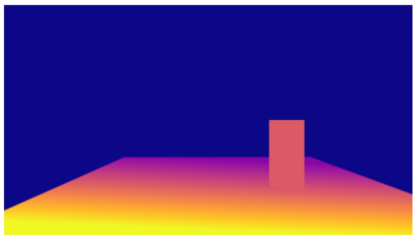

(e)

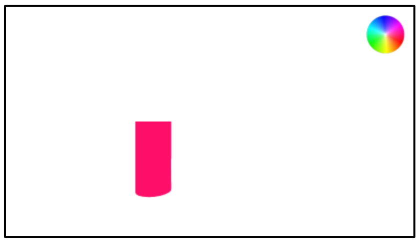

(f)

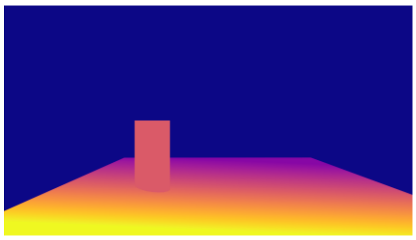

(g)

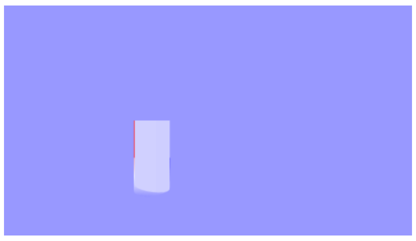

(h)

Figure 4.1 – Visual description of how disparity change can be used to assess depth flow: (a) 3D rendering of the simple scene, with some scene flow vectors and camera position; (b) l_0; (c) d_0^l; (d) l_1; (e) d_1^l; (f) f_{01}^l: optical flow map relative to l_0; (g) $r_0 d_1^l$: reprojection of d_1^l by using f_{01}^l (backwards); (h) disparity change map given by the difference between d_0^l and $r_0 d_1^l$.

4.2. Architectural hypotheses

Depending on the methodology that we use for predicting relative disparities, we distinguish between two architectures for *Pantaflow*: *mono** (mono-star) infers them by warping *Monodepth*'s predictions with *Monoflow's*, while *unison* regresses them directly.

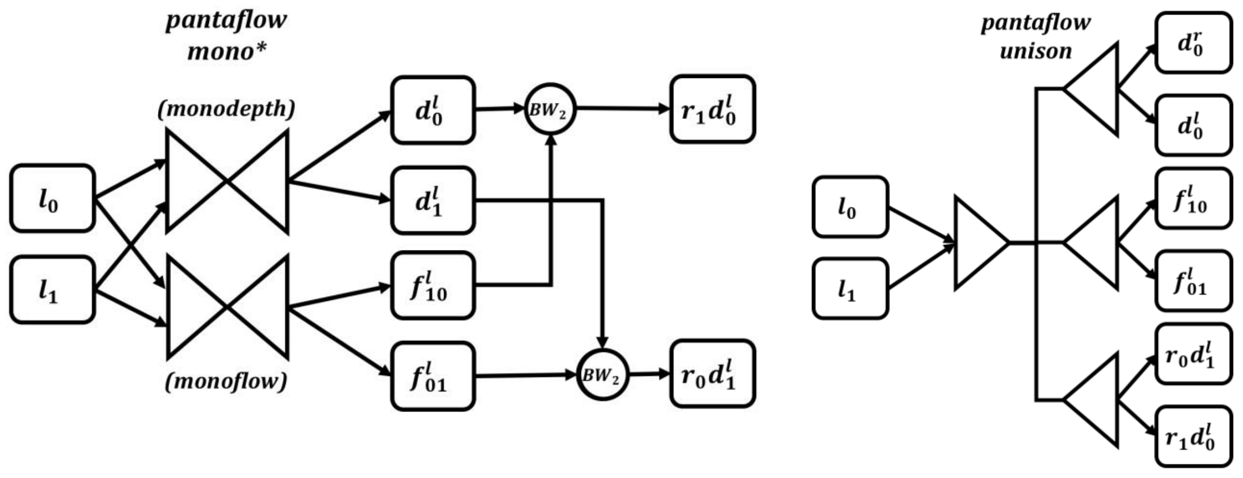

(a) (b)

Figure 4.2 – Visual comparison of the structures of the two candidate architectures for Pantaflow: mono* *(a) and* unison *(b).*

4.2.1. Mono*

The first proposed architecture for *Pantaflow* (see figure 4.2a) is called *mono** and consists of the juxtaposition of a *Monodepth*-like encoder/decoder-structured CNN and a separate *Monoflow*-like encoder/decoder-structured CNN, whose combined predictions we established to be sufficient to express *scene flow*. In order to obtain the two relative disparity maps, the portion of the net that infers depth is initially used to predict disparities for both input frames l_0 and l_1. The optical flow information that is regressed by the other sub-network is then used to re-project d_0^l and d_1^l so as to localise their values to the position of the corresponding points at time 1 and 0 respectively, yielding $r_1 d_0^l$ and $r_0 d_1^l$.

Loss gradient is computed at training time from d_0^l, d_0^r, f_{10}^l and f_{01}^l predictions exactly as in *Monodepth* and *Monoflow*. Coherently, relative disparity maps predicted at four decreasing scales and are also used as a source of loss by the means of a weighted sum between an image loss term, a smoothness loss term and a consistency loss term, as described in section 4.3.

4.2.2. Unison

The second architecture that we propose for *Pantaflow* (figure 4.2b), called *unison*, relies on a simplified organisation by factorising the encoders between the two encoder/decoder-structures that we presented in *mono**. Temporal pairs of input frames are fed into a single encoder that is then connected to three distinct decoders, in charge of inferring *disparity*, *optical flow* and *relative disparity* respectively. This means that $r_1 d_0^l$ and $r_0 d_1^l$ are not obtained through warping, but directly as products from one of the decoders. These predictions are logically employed to generate loss gradient along with the inferences coming from the other two decoders, as described in section 4.3.

4.3. Training Pantaflow

Regardless of the specific *Pantaflow* architecture employed, the network is trained by generating loss terms from the predicted disparity maps at time 0 d_0^l and d_0^r, from the inferred optical flow maps f_{10}^l and f_{01}^l and from the two relative left disparity maps $r_0 d_1^l$ and $r_1 d_0^l$. These contributions are simply added up to form the overall training loss, after dividing by two the term that relates to optical flow. This is done in order to enforce balance among the terms, as f_{10}^l and f_{01}^l have twice as many channels as the other maps and therefore generate twice as much loss gradient.

$$loss_{pantaflow} = loss_{disp} + loss_{reldisp} + \frac{loss_{optflow}}{2}$$

$loss_{disp}$ and $loss_{optflow}$ are computed like the overall losses for *Monodepth* and *Monoflow* respectively:

$$loss_{disp} = \left(loss^{l}_{image} + loss^{r}_{image}\right) \cdot image_{weight} + \left(loss^{l}_{smoothness} + loss^{r}_{smoothness}\right) \cdot smoothness_{weight} + \left(loss^{l}_{consistency} + loss^{r}_{consistency}\right) \cdot consistency_{weight}$$

$$loss_{optflow} = \left(loss^{01}_{image} + loss^{10}_{image}\right) \cdot image_{weight} + (loss^{01}_{smoothness} + loss^{10}_{smoothness}) \cdot smoothness_{weight} + \left(loss^{01}_{consistency} + loss^{10}_{consistency}\right) \cdot consistency_{weight}$$

Where the particular loss terms are the ones defined in chapters 2.3.2 and 3.1.

The contribution to loss coming from relative disparities is similarly computed as

$$loss_{reldisp} = \left(loss^{rel0}_{image} + loss^{rel1}_{image}\right) \cdot image_{weight} + \left(loss^{rel0}_{smoothness} + loss^{rel1}_{smoothness}\right) \cdot smoothness_{weight} + \left(loss^{rel0}_{consistency} + loss^{rel1}_{consistency}\right) \cdot consistency_{weight}$$

While disparities and relative disparities are very similar in that they are both always positive and ultimately express the same quantity, a novel warping procedure needs to be defined in order to use relative disparities in reprojections when we compute the *image* loss term. In the following, we will only examine the way we use $r_0 d^l_1$ to produce image loss. The equivalent contribution for $r_1 d^l_0$ is obtained by inverting all 0 and 1 indices in the formulae that will be introduced.

Since $r_0 d^l_1$ is a backward flow-warped version of the left disparity at time 1 d^l_1, it can be used to tentatively reconstruct l_1 by backward-warping r_1, in analogy with what *Monodepth* does. In order to do this, however, it is necessary to refer $r_0 d^l_1$ to time 1 by the means of a backward warping with flow f_{10}^l. The result of this warping is expressed as $\tilde{d}_1^l$ in figure 4.2 and can be used to warp r_1, thus obtaining $\tilde{\tilde{l}}_1$, which is compared with l_1 by the means of the combination of L1 and SSIM distance metrics that we already presented in chapter 3, as expressed in the formula that follows:

$$loss_{image}^{rel0} = \frac{1}{N}\sum_{i,j} \alpha \frac{1 - SSIM\left(\tilde{\tilde{l}}_1(i,j), l_1(i,j)\right)}{2} + (1-\alpha)\|\tilde{\tilde{l}}_1(i,j) - l_1(i,j)\|$$

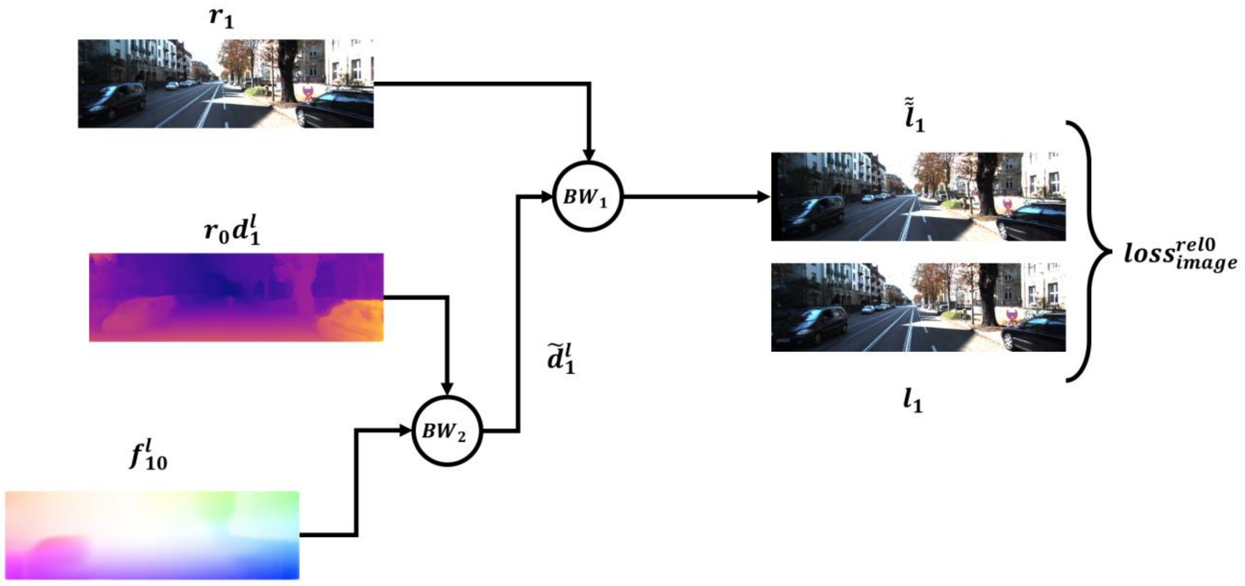

Figure 4.2 – A visual description showing how the second left frame is tentatively reconstructed by backward-warping the second right frame with warped relative disparity. The difference between reconstructed and original images is the primary source of loss.

For the term that enforces consistency between couples of predictions, we simply choose to compare $\tilde{d}_1^l$ as obtained above with the other relative disparity.

$$loss_{consistency}^{rel0} = \frac{1}{N}\sum_{i,j} |r_1 d_0^l(i,j) - \tilde{d}_1^l(i,j)|$$

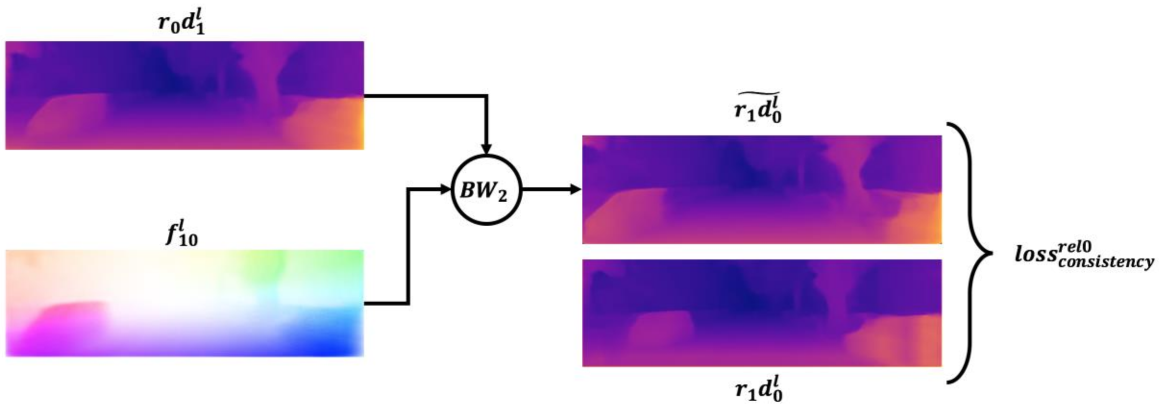

Figure 4.3 – A visual description showing the procedure for the computation of consistency loss. Notice that this is a simple one-step warping with optical flow.

Finally, the smoothness term is computed like in the previous networks, by associating a penalty to high $r_0d_1^l$ gradients which is weighted accordingly to image gradients to introduce tolerance over image discontinuities. Notice how the image we use is l_0, as $r_0d_1^l$ is expected to refer to it.

$$loss_{smoothness}^{rel0} = \frac{1}{N}\sum_{i,j}\left|\partial_x r_0 d_1^l(i,j)\right|e^{-\|\partial_x l_0(i,j)\|} + \left|\partial_y r_0 d_1^l(i,j)\right|e^{-\|\partial_y l_1(i,j)\|}$$

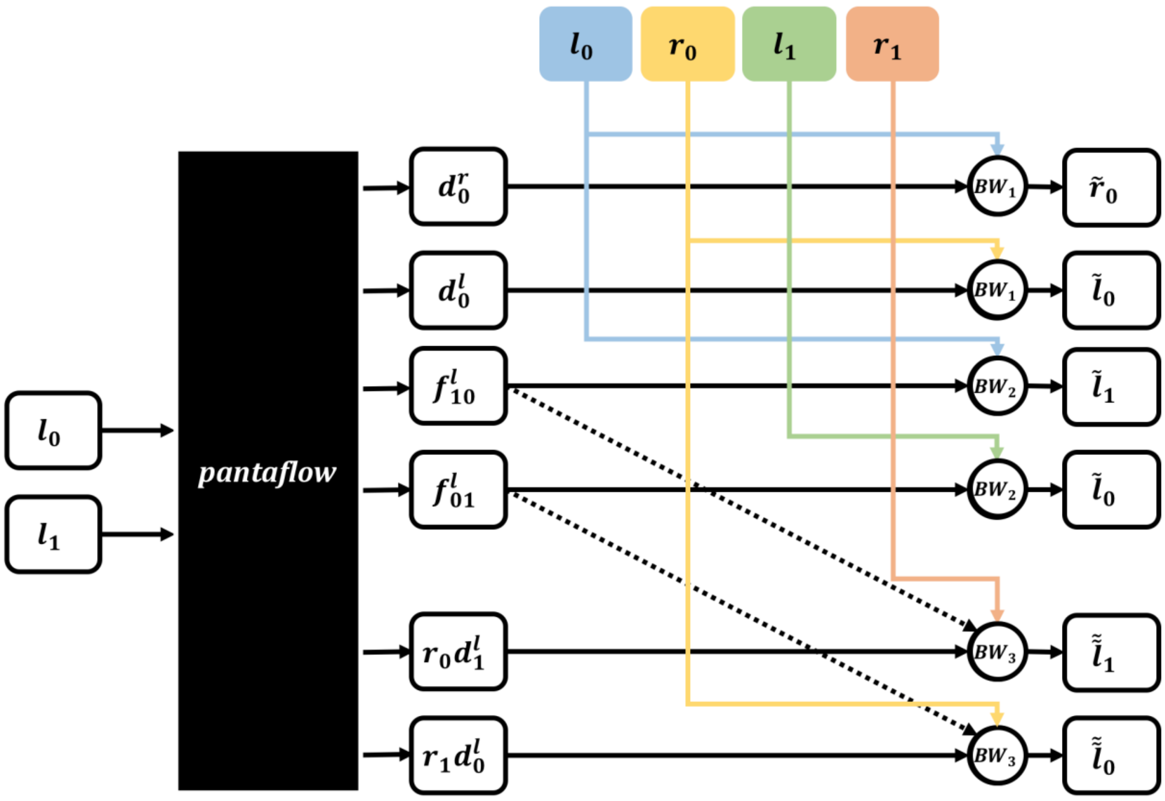

Figure 4.4 – A diagram showing how two subsequent frames referring to the same camera are used for training Pantaflow *(only image loss terms are displayed). The network is shown as a black-box as there are no differences in training tied to the specific architecture.*

5. Experimental Results

5.1. Training specifications

Training for *Pantaflow* is carried out on the KITTI dataset [4], re-organised in 28969 temporal pairs of stereo frames. Batches of 8 items are used for each iteration for a grand total of 181100 iterations, corresponding to 50 epochs approximately.
An NVIDIA Titan X Graphic Processor equipped with 12 GB of RAM was used for both training and testing.

5.2. Post-Processing

An additional post-processing step similar to the one carried out by Godard et al. in [3] is applied to disparity, optical flow and relative disparity predictions by *Pantaflow*. Each prediction is separately computed both for the input temporal pair l_0, l_1 and its flipped version l_0^{flip}, l_1^{flip}. Let p be the resulting prediction that relates to the former pair, p^{flip} be the one relating to the latter pair and p^{avg} be their average, they are combined as follows (see figure 5.1):

- The leftmost 5% of the post-processed result is sampled from p.
- The rightmost 5% of the post-processed result is sampled from p^{flip}.
- The remaining is sampled from p^{avg}

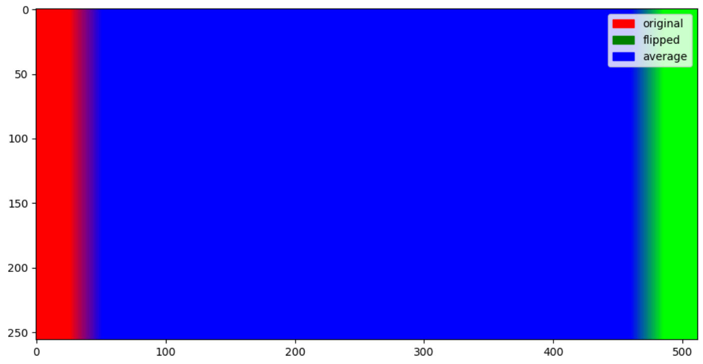

Figure 5.1 – visualisation of the combination of results for posts processing.

5.3. Results and Comparisons

This section contains a quantitative evaluation of the test of *Pantaflow* on the 2015 extension to the KITTI dataset [13]. This dataset is used as a reference as it comprehensively includes ground truth data for disparity, optical flow and scene flow. Results for these three types of inference are presented separately comparing the two architectures for the proposed network. Where suitable, additional comparisons will be made with other existing studies.

5.3.1. Disparity Inference

To quantify *Pantaflow*'s performances as regards disparity map regression, we employ the same evaluation code provided by *Godard et al.* in [3] and we compare our results directly with the one presented in their paper.

The following evaluation metrics are used:

- Absolute Relative Difference (**Abs Rel**): the absolute mismatch between a ground truth value v and its prediction $\tilde{v}$, divided by v in order to further penalise errors when attempting to predict higher values. This is averaged out by dividing by the total number of pixels N.

$$\frac{1}{N}\sum_{i,j}\frac{\left|v_{i,j}-\tilde{v}_{i,j}\right|}{v_{i,j}}$$

- Squared Relative Difference (**Sq Rel**): similar to the one above, squaring the difference between v and $\tilde{v}$.

$$\frac{1}{N}\sum_{i,j}\frac{\left(v_{i,j}-\tilde{v}_{i,j}\right)^2}{v_{i,j}}$$

- Root Mean Squared Error (**RMSE**): the square root of the average of the squared mismatches between v and $\tilde{v}$.

$$\sqrt{\frac{1}{N}\sum_{i,j}\left(v_{i,j}-\tilde{v}_{i,j}\right)^2}$$

- Logarithmic Root Mean Squared Error (**RMSE log**): the one above, where predictions are compared after applying logarithmic function. As $\log v - \log \tilde{v} = \log \frac{v}{\tilde{v}}$, this metric is much more sensitive to larger differences.

$$\sqrt{\frac{1}{N}\sum_{i,j}\left(\log v_{i,j}-\log \tilde{v}_{i,j}\right)^2}$$

- Outliers percentage: a metric computing the percentage of outliers, meaning points for which the mismatch between the ground truth value v and the predicted value $\tilde{v}$ exceeds a given absolute threshold t_a and the ratio between the mismatch and the ground truth value exceeds a given relative threshold t_r. In the following, we assume $t_a = 3.0$ and $t_r = 0.05$ for the Absolute and Relative Outlier percentage (**AROP**, also known as **D1-all**) and $t_a = 3.0$ and $t_r = 0$ for the Absolute Outliers Percentage (**AOP**), which expresses this metric disregarding the relative threshold).

$$\frac{1}{N}\sum_{i,j}\gamma_{i,j}, \qquad where\, \gamma_{i,j} = \begin{cases} 1\ if\ \left|v_{i,j}-\tilde{v}_{i,j}\right| \geq t_a\ and\ \dfrac{\left|v_{i,j}-\tilde{v}_{i,j}\right|}{\tilde{v}_{i,j}} \geq t_r \\ 0 \end{cases}$$

- Thresholded errors ($\boldsymbol{\delta < t}$): the percentage of predictions such that their relative size with respect to ground truth (expressed by the maximum between $\frac{v}{\tilde{v}}$ and $\frac{\tilde{v}}{v}$) is lower than a threshold t. In our evaluation, we consider $t \in \{1.25, 1.25^2, 1.25^3\}$.

$$\frac{1}{N}\sum_{i,j}\delta_{i,j}\,, \qquad where\ \delta_{i,j} = \begin{cases} 1\ if\ \max\left(\frac{v_{i,j}}{\tilde{v}_{i,j}}, \frac{\tilde{v}_{i,j}}{v_{i,j}}\right) < t \\ 0 \qquad\qquad else \end{cases}$$

The results that are presented in table 5.1 confirm that *Pantaflow-mono** outperforms *Monodepth* with respect to almost every metric, indicating that taking into account optical flow and scene flow information during training allows for a slight, yet consistent, improvement. Note that this comparison cannot take post-processing into account, as [3] only provides post-processed data for models trained on the KITTI dataset [4] and the Cityscapes dataset [20], while *Pantaflow* is only trained on the former.
Additionally, it is shown that *mono** steadily obtains better scores than *unison*.

Method	*Abs Rel*	*Sq Rel*	*RMSE*	*RMSE log*	*AROP*	$\delta < 1.25$	$\delta < 1.25^2$	$\delta < 1.25^3$
Monodepth	0.124	1.388	**6.125**	0.217	**0.303**	0.841	0.936	**0.975**
unison	0.153	2.097	7.016	0.253	0.377	0.793	0.911	0.963
*mono**	**0.122**	**1.347**	6.172	**0.215**	0.310	**0.843**	**0.937**	**0.975**
unison pp	0.147	1.905	6.709	0.243	0.376	0.796	0.915	0.966
mono pp*	**0.116**	**1.160**	**5.845**	**0.206**	**0.305**	**0.846**	**0.943**	**0.978**

Lower is better | Higher is better

Table 5.1 – Quantitative evaluation of Pantaflow and Monodepth for disparity inference on the 2015 extension to the KITTI dataset.

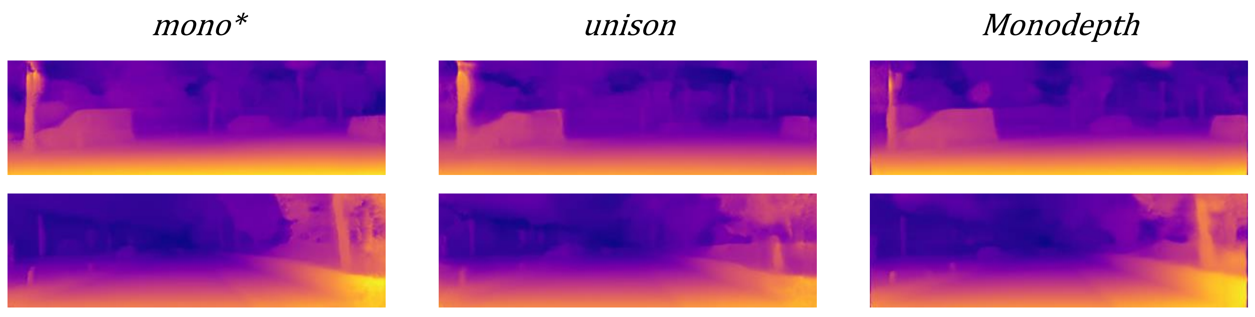

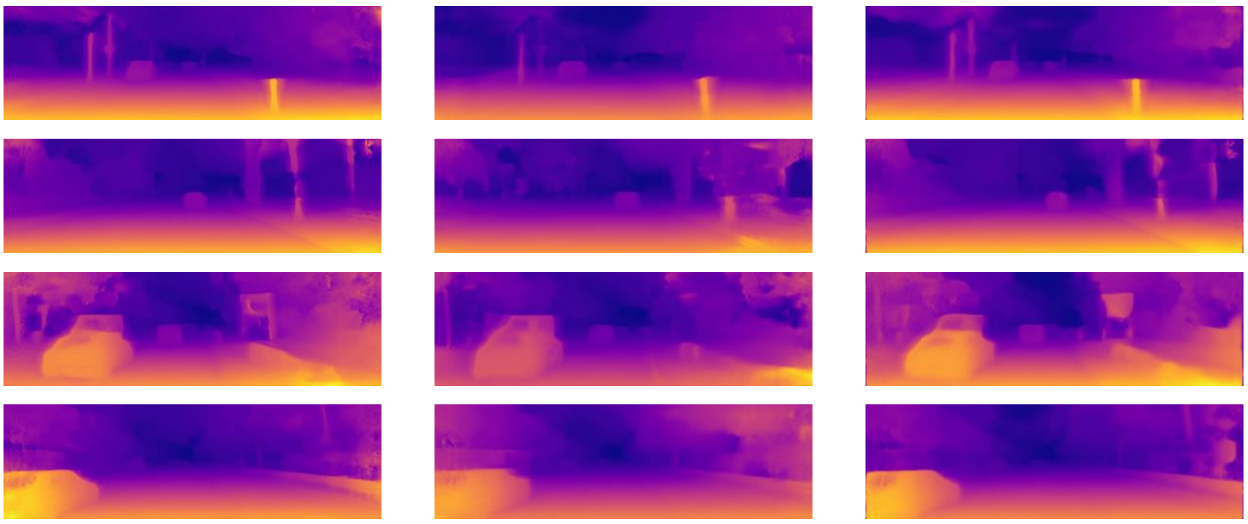
Figure 5.2 – Qualitative comparison for disparity maps as predicted by mono*, unison *and* Monodepth.

5.3.2. Optical Flow Inference

As far as optical flow inference is concerned, we draw a comparison between *Pantaflow* and *Monoflow* in terms of the aforementioned Absolute Outlier Percentage and on the Average Endpoint Error (**EPE**). Notice that, since flow is a two-dimensional quantity, the mismatch between the ground truth value $v = (v^x, v^y)$ and predicted value $\tilde{v} = (\tilde{v}^x, \tilde{v}^y)$ is computed by the means of the Euclidean distance.

$$EPE(v, \tilde{v}) = \frac{1}{N} \sum_{i,j} \sqrt{\left(v_{i,j}^x - \tilde{v}_{i,j}^x\right)^2 + \left(v_{i,j}^y - \tilde{v}_{i,j}^y\right)^2}$$

$$AOP(v, \tilde{v}) = \frac{1}{N} \sum_{i,j} \gamma_{i,j}\,, \quad where\ \gamma_{i,j} = \begin{cases} 1\ if\ \sqrt{\left(v_{i,j}^x - \tilde{v}_{i,j}^x\right)^2 + \left(v_{i,j}^y - \tilde{v}_{i,j}^y\right)^2} \geq 3.0 \\ 0 \end{cases}$$

The results that can be found in table 5.2 confirm that Pantaflow outperforms *Monoflow*. This suggests that tackling disparity, relative disparity and optical flow prediction within the same end-to-end training allows for the obtainment of better results. It must be noted that *mono** outperforms *unison* in this task as well.

Method	Occluded		Non-occluded	
	Epe	AOP	Epe	AOP
Monoflow	24.057	0.680	18.017	0.632
unison	22.220	0.638	14.860	0.581
mono*	**19.685**	**0.510**	**11.988**	**0.434**
Monoflow pp	23.084	0.688	16.909	0.640
unison pp	21.476	0.631	14.679	0.574
mono* pp	**18.686**	**0.506**	**11.453**	**0.430**

Lower is better	Higher is better

Table 5.2 – Quantitative evaluation of Pantaflow and Monoflow for optical flow prediction on the 2015 extension to the KITTI dataset.

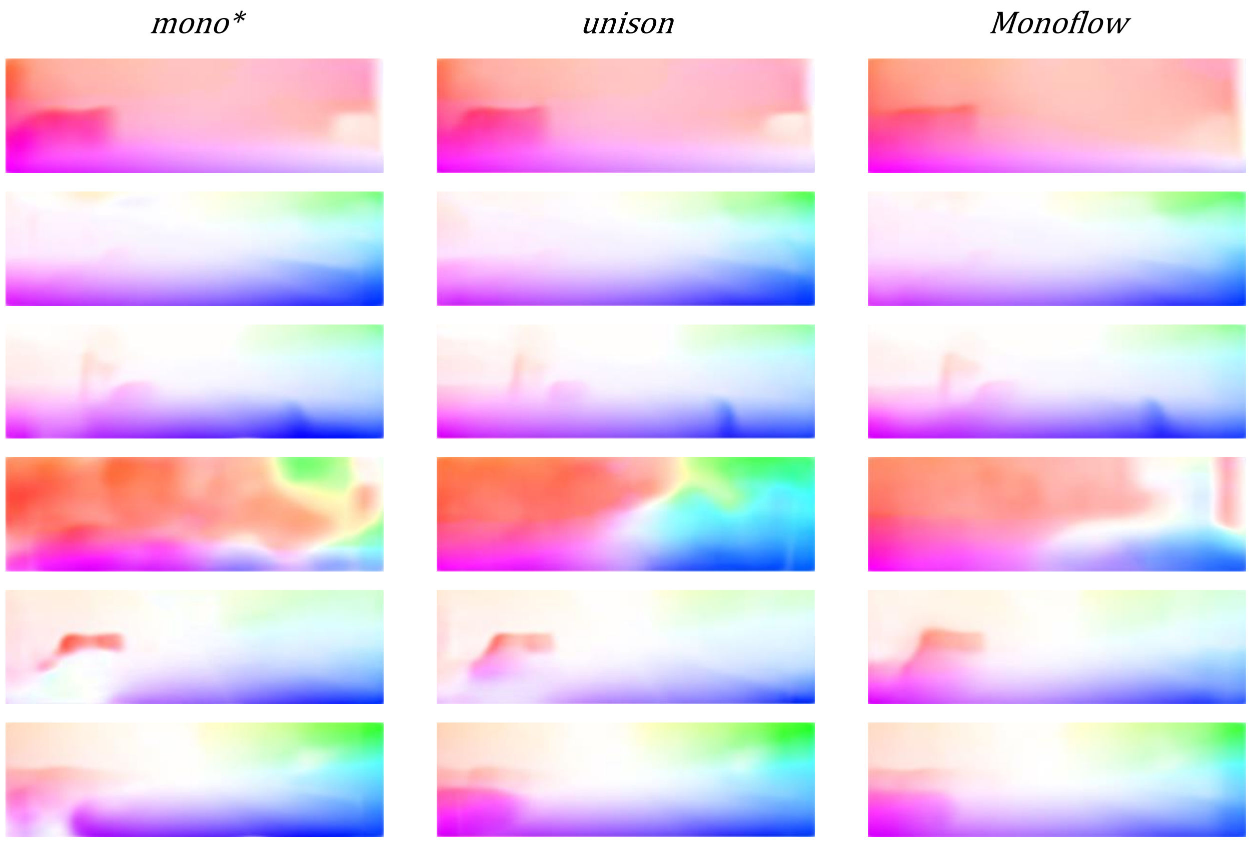

Figure 5.3 – Qualitative comparison for optical flow predictions by mono*, unison and Monoflow.

5.3.3. Scene Flow Inference

To account for the performances of the network with respect to scene flow, we firstly evaluate how good it is at predicting relative disparity. This can be quantified by computing the same evaluation metrics used for disparity by taking $r_0 d_1^l$ into account. The results are listed in table 5.3.

Although there are not suitable architectures available for a comparison in literature, it is once again confirmed that *mono** proves to be more effective than *unison*. In figure 5.4, we show a qualitative comparison between relative disparities $r_0 d_1^l$ predicted by the two architectures.

Method	*Abs Rel*	*Sq Rel*	*RMSE*	*RMSE log*	*AROP*	$\delta < 1.25$	$\delta < 1.25^2$	$\delta < 1.25^3$
unison	0.238	2.633	7.621	0.299	0.624	0.633	0.900	0.957
*mono**	**0.234**	**2.255**	**7.102**	**0.287**	**0.589**	**0.641**	**0.909**	**0.962**
unison pp	0.227	2.256	7.272	0.287	0.614	0.645	0.907	0.961
mono pp*	**0.223**	**1.911**	**6.653**	**0.274**	**0.580**	**0.650**	**0.916**	**0.968**

Lower is better	Higher is better

Table 5.3 – Quantitative evaluation of Pantaflow's architectures for relative disparity inference on the 2015 extension to the KITTI dataset.

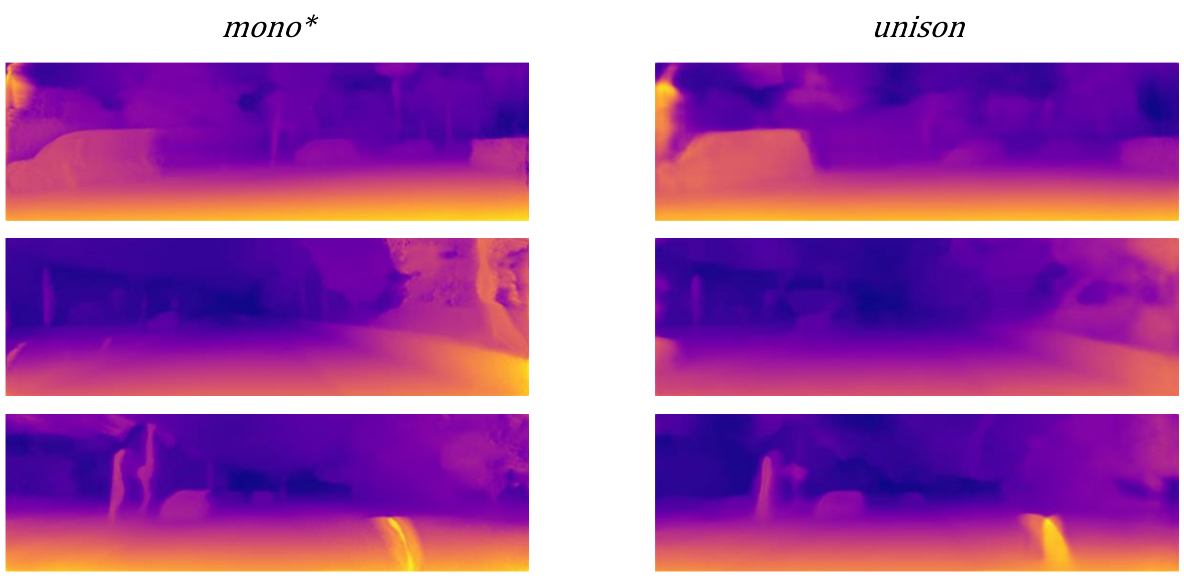

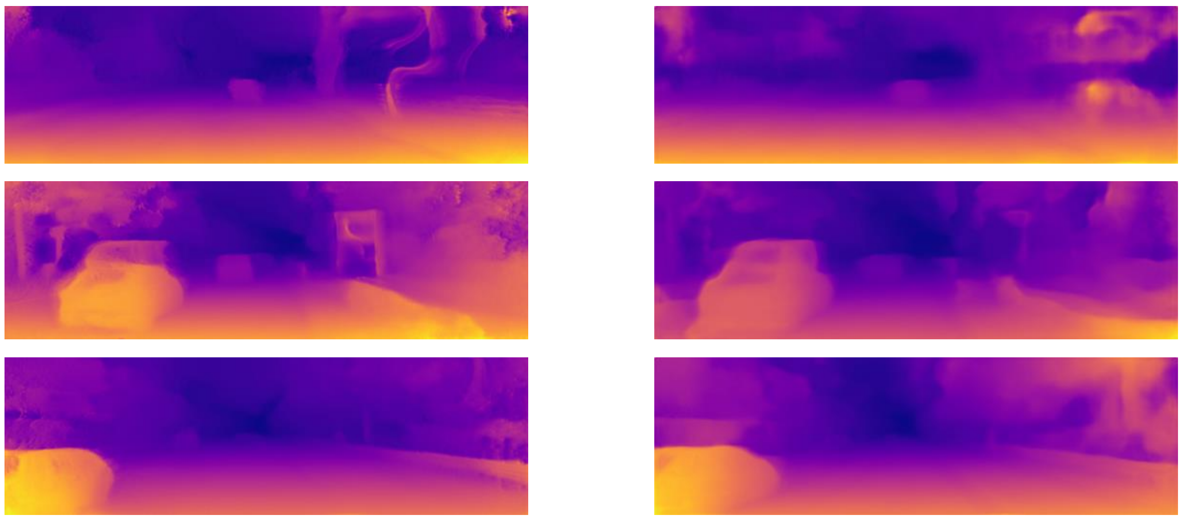
Figure 5.4 – Qualitative comparison between $r_0 d_1^l$ quantities as predicted by mono* *and* unison.

Figure 5.5 contains a visualisation of the difference between disparities at time 0 d_0^l and their relative equivalent at time 1 $r_0 d_1^l$, which is called *disparity change* and expresses points' movements along the orthogonal axis to the image plane.

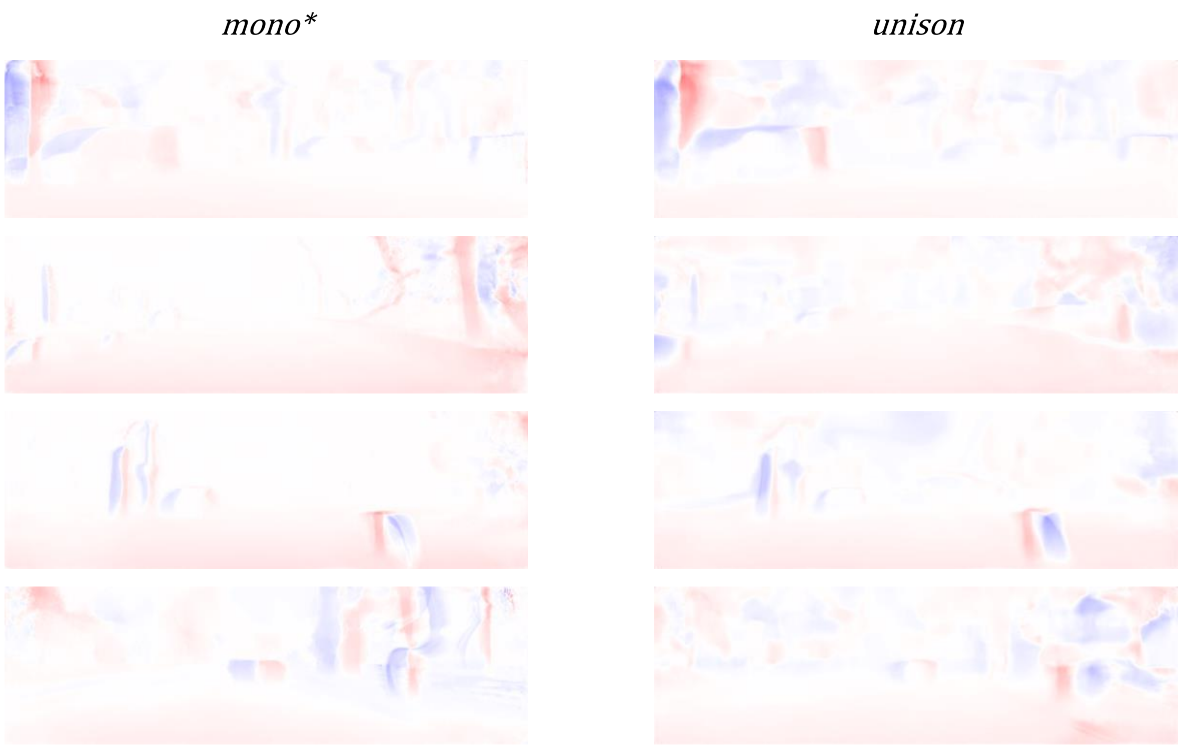

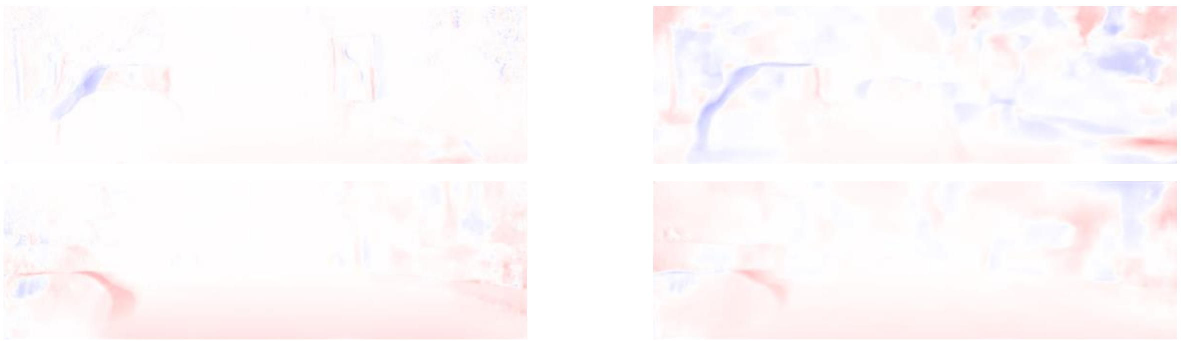
Figure 5.5 – Qualitative comparison between disparity changes as predicted by mono* *and* unison.

As it is desirable to have an overall performance index on scene flow inference, we calculate a scene flow *Absolute Outlier Percentage* by regarding as outlier any pixel that exceeds the fixed *AOP* threshold with respect to disparity, relative disparity or optical flow.
The results, which are listed in table 5.4, can be compared against the competitors in the *KITTI 2015 scene flow benchmark competition* [24], although it must be noted that no disclosed competitor makes use of unsupervised monocular prediction techniques.

Method	*d0-AOP (D1-all)*	*r0d1-AOP (D2-all)*	*f-AOP (Fl-all)*	*sf-AOP (SF-ALL)*
unison	0.386	0.622	0.581	0.676
*mono**	0.317	0.586	0.434	**0.541**
unison pp	0.386	0.612	0.574	0.672
mono pp*	0.313	0.576	0.430	**0.536**

Lower is better	Higher is better

Table 5.4 – Quantitative evaluation of Pantaflow’s *architectures in terms of percentage outliers for separate and joint prediction of disparity, relative disparity and optical flow. Each metric presents its equivalent name used in [24] in parentheses.*

6. Conclusions and Future Developments

In this thesis, a novel neural network model capable of performing unsupervised monocular scene flow prediction was developed. To the best of the author's knowledge, no published attempt has been made to predict this quantity without supervision by the means of an end-to-end trained model and the broad majority of the existing state-of-the-art techniques have ostensibly longer execution times. The improvement we obtain with respect to [3] confirms that disparity map inference benefits from being tackled side-by-side with optical flow and relative disparity prediction.

While availability of *Pantaflow* represents a meaningful step towards the achievement of real-time scene flow prediction, possibly leading to important improvements in many applicative areas, there is definitely room for the attainment of better results via architectural improvements and finer tuning as follows:

- Alternative architectures like *FlowNet*, that have already proved successful for inferring optical flow, might be deployed and trained along with *MonoDepth* to predict scene flow.
- Experimentations can be made by considering different combinations of image difference functions in training (e.g. using Census for all image losses).
- According to very recent studies [25], self-supervised training of Encoder/Decoder-structured CNNs might benefit from the loss function being computed for images at full-scale. Tests could be made by up-sampling the predictions that we extract from the deeper layers of the decoder prior to comparing them with the ground truth.

7. References

[1] S. Vedula, S. Baker, P. Rander, R. Collins and T. Kanade. Three-dimensional scene flow. In Proceedings of the Seventh IEEE International Conference on Computer Vision, volume 2, pages 722–729, 1999.

[2] F. Huguet and F. Devernay. A variational method for scene flow estimation from stereo sequences. In Computer Vision, 2007. ICCV 2007. IEEE 11th International Conference on, pages 1–7. IEEE, 2007.

[3] C. Godard, O. Mac Aodha and G. J. Brostow. Unsupervised monocular depth estimation with left-right consistency. In Computer Vision and Pattern Recognition, 2017.

[4] A. Geiger, P. Lenz and R. Urtasun. Are we ready for autonomous driving? The kitti vision benchmark suite. In Conference on Computer Vision and Pattern Recognition (CVPR), 2012.

[5] A. Dosovitskiy, P. Fischer, E. Ilg, P. Hausser, C. Hazirbas, V. Golkov, P. van der Smagt, D. Cremers and T. Brox. Flownet: Learning optical flow with convolutional networks. In the IEEE International Conference on Computer Vision (ICCV), December 2015.

[6] H. Zhao, O. Gallo, I. Frosio and J.Kautz. Loss Functions for Neural Networks for Image Processing. ArXiv e-prints, Nov. 2015.

[7] C. Vogel, K. Schindler and S. Roth. 3d scene flow estimation with a piece-wise rigid scene model. International Journal of Computer Vision, 115(1):1–28, 2015.

[8] R. Zabih and J. Woodfill. Non-parametric local transforms for computing visual correspondence. In ECCV 1994.

[9] J. Flynn, I. Neulander, J. Philbin and N. Snavely. Deepstereo: Learning to predict new views from the world's imagery. In CVPR, 2016.

[10] J. Zbontar and Y. LeCun. Computing the stereo matching cost with a convolutional neural network. In Conference on Computer Vision and Pattern Recognition (CVPR), 2015.

[11] N. Mayer, E. Ilg, P. Häusser, P. Fischer, D. Cremers, A. Dosovitskiy and T. Brox. A large dataset to train convolutional networks for disparity, optical flow, and scene flow estimation. In the IEEE Conference on Computer Vision and Pattern Recognition (CVPR), 2016.

[12] T. Taniai, S. N. Sinha and Y. Sato. Fast multi-frame stereo scene flow with motion segmentation. In the IEEE Conference on Computer Vision and Pattern Recognition (CVPR), July 2017.

[13] M. Menze and A. Geiger. Object scene flow for autonomous vehicles. In Conference on Computer Vision and Pattern Recognition (CVPR), 2015.

[14] M. Poggi and S. Mattoccia. Learning to predict stereo reliability enforcing local consistency of confidence maps. IEEE Conference on Computer Vision and Pattern Recognition (CVPR 2017), Jul. 2017.

[15] A. Tonioni, M. Poggi, L. Di Stefano and S. Mattoccia. Unsupervised Adaptation for Deep Stereo. IEEE International Conference on Computer Vision (ICCV 2017), Oct. 2017.

[16] M. Bai, W. Luo, K. Kundu and R. Urtasun. Exploiting semantic information and deep matching for optical flow. In European Conference on Computer Vision, pages 154–170. Springer, 2016.

[17] A. Behl, O. H. Jafari, S. K. Mustikovela, H. A. Alhaija, C. Rother and A. Geiger. Bounding boxes, segmentations and object coordinates: How important is recognition for 3d scene flow estimation in autonomous driving scenarios? In International Conference on Computer Vision (ICCV), 2017.

[18] F. Stein. Efficient computation of optical flow using the census transform. In DAGM 2004.

[19] D. Sun, S. Roth and M. J. Black. A Quantitative Analysis of Current Practices in Optical Flow Estimation and the Principles Behind Them. In the International Journal of Computer Vision, Volume 106, pp. 115-137. Jan. 2014.

[20] M. Cordts, M. Omran, S. Ramos, T. Rehfeld, M. Enzweiler, R. Benenson, U. Franke, S. Roth and B. Schiele. The cityscapes dataset for semantic urban scene understanding. In CVPR, 2016.

[21] Y. Wang, Y. Yang, Z. Yang, L. Zhao, P. Wang and W. Xu. Occlusion Aware Unsupervised Learning of Optical Flow. ArXiv e-prints, Nov. 2017.

[22] E. Ilg, N. Mayer, T. Saikia, M. Keuper, A. Dosovitskiy and T. Brox. FlowNet 2.0: Evolution of Optical Flow Estimation with

Deep Networks. In IEEE Conference on Computer Vision and Pattern Recognition (CVPR), Jul. 2017.

[23] S. Meister, J. Hur and S. Roth. UnFlow: Unsupervised Learning of Optical Flow with a Bidirectional Census Loss, in AAAI, Feb. 2018

[24] The benchmark refers to [13] and can be found at http://www.cvlibs.net/datasets/kitti/eval_scene_flow.php.

[25] C. Godard, O. M. Aodha, G. J. Brostow. Digging into self-supervised monocular depth estimation. ArXiv e-prints, Jun. 2018.

[26] Xie, R. Girshick and A. Farhadi. Deep3d: Fully automatic 2d-to-3d video conversion with deep convolutional neural networks. In ECCV, 2016.

[27] M. Poggi, F. Aleotti, F. Tosi, S. Mattoccia. Towards real-time unsupervised monocular depth estimation on CPU. Accepted at IEEE/RSJ International Conference on Intelligent Robots and Systems (IROS 2018), Madrid, Spain, October, 1-5, 2018.